

RESEARCH ARTICLE

[View Article Online](#)
[View Journal](#)Cite this: DOI: 10.1039/
d5md00264hNovel mangiferin derivatives attenuate
adipogenesis in 3T3-L1 preadipocytes and
ameliorate diet induced obesity in C57BL/6J mice†Dong-Quan Gu,^a Yin Li,^a Liu-Shun Wu,^a Meng-Ting Lyu,^a Ying Li,^a
Sheng-Zhuo Huang,^d Feng-Qing Xu,^{*abc} De-Ling Wu^{*abc} and Wu-Xi Zhou ^{*ab}

Mangiferin with a xanthone scaffold exhibited potent anti-obesity activities and thus has attracted interest. However, some shortcomings, including limited solubility and moderate potency, restrict its application. To develop novel and efficient anti-obesity agents, a series of mangiferin (MGF) amino acid derivatives were synthesized, optimized and evaluated for anti-obesity activities *in vitro* and *in vivo*. Among these derivatives, **G1** was identified to be a promising compound. **G1** showed better liposolubility compared to MGF. In 3T3-L1 preadipocytes, **G1** significantly inhibited cell differentiation and reduced fat accumulation by increasing inhibitory activity on fatty acid synthase, and triggering G0/G1 phase cell cycle arrest and production of intracellular reactive oxygen species. The intraperitoneal administration of **G1** (30, 60 mg kg⁻¹/2 days) significantly inhibited body, liver and fat tissue weight gain, reduced lipid dysfunction, and ameliorated pathological characteristics in high-fat diet induced C57BL/6J obese mice. These results suggest that compound **G1** may warrant further investigation as a promising anti-obesity agent for the treatment of human obesity.

Received 27th March 2025,
Accepted 20th June 2025

DOI: 10.1039/d5md00264h

rsc.li/medchem

1. Introduction

Obesity, as a significant risk factor for many metabolic diseases,^{1,2} is closely related to lipid dysfunction, which can cause superfluous endogenous fatty acids by increasing *de novo* lipogenesis and frequently progresses to hyperlipidemia and fatty liver.^{3,4} Inhibition of fatty acid synthase (FASN) has been shown to have a therapeutic effect on obesity.^{5–7} FASN helps the body to produce the saturated fatty acid palmitate, which can be further converted to the monounsaturated fatty acid palmitoleate in the body. Currently, anti-obesity drugs developed based on fatty acid synthesis are relatively scarce.^{8–10}

Mangiferin (MGF, Fig. 1) is a natural xanthone glucoside found in mango trees, exhibiting a wide range of pharmacological activities.¹¹ More interestingly, MGF was found to regulate multiple lipid metabolism-related

biological processes, including the production of total cholesterol (TC), triglyceride (TG), low-density lipoprotein cholesterol (LDL-C) and high-density lipoprotein cholesterol (HDL-C), and related protein expression, which makes MGF a promising drug for the treatment of obesity.^{12,13} However, the limited solubility and moderate anti-obesity activity of MGF have restricted its development and application.^{14,15} According to the Biopharmaceutics Classification System (BCS), MGF is classified as BCS class 4, indicating that it is a low solubility and low permeability compound.¹⁶ This poor solubility results in poor transmembrane permeability, low bioavailability and limited activity of MGF. At present, the main methods to improve the solubility of MGF are to prepare some physically or chemically modified derivatives. Physically modified derivatives are mainly made into some special preparations, such as microemulsion, nanoparticles, etc.^{17,18} Although these physical methods can improve the water solubility of MGF well, the equipment requirements are high, the production price is expensive and there are potential toxicity risks.¹⁹ Chemically modified derivatives are

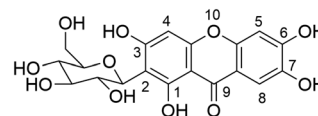


Fig. 1 Chemical structure of MGF.

^a School of Pharmacy, Anhui University of Chinese Medicine, Hefei, 230012, PR China. E-mail: xufengqing@ahtcm.edu.cn, dlwu7375@ahtcm.edu.cn, zhouwuxi@ahtcm.edu.cn^b Anhui Province Key Laboratory of Bioactive Natural Products, Hefei, 230012, PR China^c Anhui Province Key Laboratory of New Manufacturing Technology for Traditional Chinese Medicine Decoction Pieces, Hefei, 230012, PR China^d Key Laboratory of Research and Development of Natural Product from Li Folk Medicine of Hainan Province, Chinese Academy of Tropical Agricultural Sciences, Institute of Tropical Bioscience and Biotechnology, Haikou, 571101, PR China† Electronic supplementary information (ESI) available. See DOI: <https://doi.org/10.1039/d5md00264h>

mainly subjected to certain changes in chemical structure, such as salting, alkylation, acylation, *etc.*^{20,21} Although these chemical modification methods have improved the solubility of MGF to some extent, the therapeutic effect of existing derivatives is still not satisfactory. Therefore, optimizing this scaffold is of great necessity.

Amino acids as the building blocks of life regulate lots of biological processes, including regulation of the lipid profile.^{22,23} Amino acid derivatives of many lead compounds have gained popularity due to their significant improvement in solubility, bioavailability and biological activity but low adverse effects.^{24,25} Recently, many lead compounds have been produced by incorporating amino acids which showed good solubility and high pharmacological activity, indicating that amino acids have broad application prospects in the structural modification of lead compounds.^{26–28} In the present study, we introduced amino acids as functional groups into MGF to design and synthesize a series of novel amino acid derivatives regulating solubility and lipid metabolism. Furthermore, the anti-obesity action and pharmacological mechanisms of the most potent compound (G1) were explored *in vitro* and *in vivo*.

2. Results and discussion

2.1 Design of MGF derivatives

Most of the environment in the human body is a water-based environment, which requires drugs to have a certain hydrophilicity; body biofilms are composed of phospholipids, which require drugs to have a certain lipophilicity. High or low hydrophilicity or lipophilicity of drugs may have adverse effects on drug transport and absorption. It was reported that the poor lipophilicity of MGF and its derivatives leads to a slow absorption rate, further resulting in low blood concentrations.^{29,30} The lipophilic derivatives of lots of lead compounds enhance pharmacological activity and thus have attracted interest.³¹ In our study, the structural modification of MGF was mainly focused on the enhancement of lipophilicity. Many factors were considered in the modification process. (1) Selection of chemical reaction sites. There are four phenolic hydroxyl groups in the structure of the lead compound MGF. The 1-position phenol hydroxyl group forms a hydrogen bond with the 9-position carbonyl group, resulting in low reactivity. Therefore, structural modifications were performed on phenol hydroxyl groups at positions 3, 6 and 7. The lipophilicity of derivatives with full substitution of reaction sites will be improved the most. (2) Selection of substituent groups. In this study, 8 amino acids containing non-polar and hydrophobic groups were selected, including alanine, valine, leucine, isoleucine, proline, methionine, tryptophan and phenylalanine. The carboxyl group in their structure is formed into methyl ester, which greatly increases the lipophilicity of the groups while preserving the amino acid skeleton. (3) Selection of linkers. The linker chain is important for the introduction of amino acids. The full carbon chain not only could adjust the spatial structure of the molecule, but also could improve the lipophilicity.

2.2 Chemistry

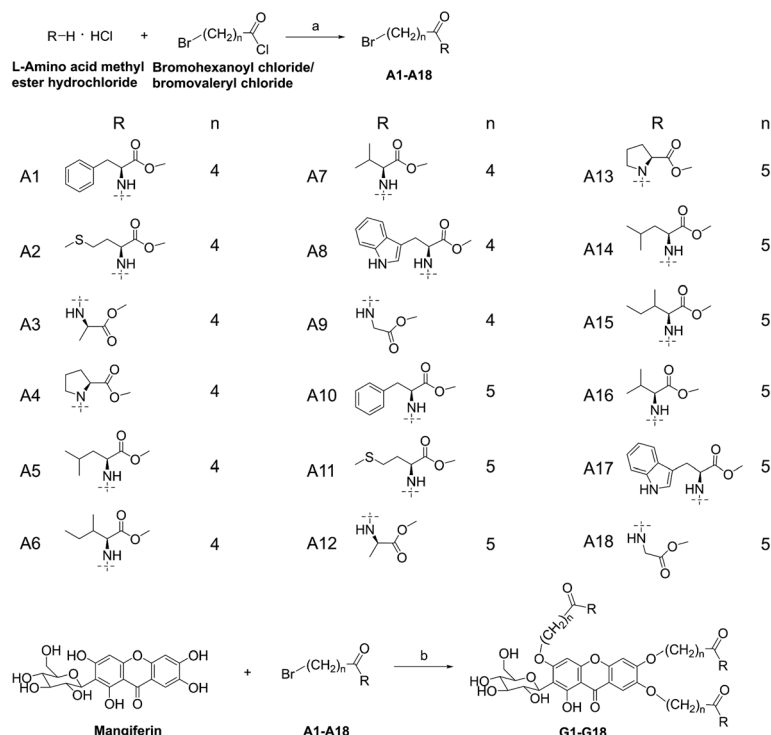
The synthetic route to the intermediates **A1–A18** and compounds **G1–G18** is exhibited in Scheme 1 and detailed in the Experimental section. Initially, amino acid methyl ester hydrochloride (L-phenylalanine methyl ester hydrochloride, L-methionine methyl ester hydrochloride, L-alanine methyl ester hydrochloride, L-proline methyl ester hydrochloride, L-leucine methyl ester hydrochloride, L-isoleucine ester hydrochloride, L-valine methyl ester hydrochloride, L-tryptophan methyl ester hydrochloride or L-glycine methyl ester hydrochloride) was acylated with 5-bromovaleryl chloride or 6-bromohexanoyl chloride in dry dichloromethane under an ice bath condition to give the intermediates with high yields. Subsequently, the intermediates were treated with MGF in the presence of K₂CO₃ in DMF at 80 °C to obtain compounds **G1–G18**.

2.3 Inhibitory activity of MGF derivatives on 3T3-L1 cells and structure–activity relationship analysis

3T3-L1 preadipocytes are a widely used *in vitro* model for research of fat metabolism, mechanism of obesity development and treatment of weight loss drugs. Therefore, we screened the inhibitory activities of MGF derivatives on 3T3-L1 cells. The anti-proliferative activity of the derivatives against 3T3-L1 preadipocytes was determined by MTT assay, and the IC₅₀ values are presented in Table 1. Obviously, the current results showed that all the derivatives exhibited superior inhibitory activity to that of MGF. As shown in Table 1, compounds **G1**, **G8**, **G10** and **G17** containing a benzene ring and indole improved the inhibition activity; the activities of derivatives **G2** and **G11** of sulfur-containing amino acids are more enhanced than those of the derivatives of saturated aliphatic chain amino acids. The activities of amino acid derivatives **G4** and **G13** containing cyclic structures can also be better enhanced. The above results indicate that the electron cloud density and unsaturation of functional groups have a significant influence on the activity of MGF derivatives. Further, the inhibitory activity of **G1** and **G10** was superior to that of **G2** and **G17**, which indicated that the number of carbons in the aliphatic chain of the connecting arm had an impact on the inhibitory activity. So far, compound **G1** displayed the most potent activity with an IC₅₀ value of 39.13 ± 0.82 μM against 3T3-L1 cells, being more active than MGF (IC₅₀ = 458.99 ± 9.50 μM) and similar to that of orlistat (64.55 ± 2.11 μM).

2.4 Solubility of MGF derivatives

The solubility of the compounds in *n*-octanol was determined by the shake flask method, and the results are presented in Table 1. The results exhibited that the equilibrium solubility of all the compounds was improved. Among them, compound **G1** was 85-fold better than MGF. Furthermore, the liposolubility of the derivatives was evaluated using the octanol/water partition coefficient (log *P*). The log *P* value for compound **G1** was 1.34, while that for MGF was 0.02.



Scheme 1 Synthesis of MGF derivatives. Reagents and conditions: (a) Et₃N, CH₂Cl₂, 0 °C, 3–6 h. (b) K₂CO₃, DMF, 80 °C, 12–18 h.

According to the results of anti-proliferative activity and solubility, compound **G1** deserved further study as a promising anti-obesity agent.

2.5 FASN inhibitory activity and molecular docking studies

To investigate whether the representative MGF derivative **G1** was efficacious against *de novo* lipogenesis, the inhibition effects of compound **G1** on FASN was determined using a FASN activity assay kit. FASN is a key enzyme in lipogenesis, catalyzing the synthesis of saturated fatty acid palmitate. As shown in Fig. 2A, **G1** could significantly inhibit FASN activity in a dose-dependent manner on the 3T3-L1 cell line, being more potent than MGF.

To study binding pattern of **G1** with FASN, molecular docking studies was carried out. The highest-scoring binding modes of MGF and **G1** show that both bind to the MAT (malonyl/acetyltransferase) domain, occupying the binding site of the natural substrate acyl-CoA (Fig. 2B). For MGF, its core framework is embedded in a hydrophobic cavity formed by Met620, Cys642, Ala622, Val675, and Leu766, forming hydrophobic interactions. Its hydroxyl and carbonyl groups can form three hydrogen bonds with Thr650, Asn644, and Arg676. Additionally, the glycosidic group at the end of MGF forms three extra hydrogen bonds with the backbone or side chains of Gly500, Gln502, and Arg787. These interactions work together to maintain the stable binding of MGF in the binding pocket. For **G1**, it can form contacts with more amino acid residues, including Met499, Gly498, Ile549, Phe553, Leu582, Val585, Met620, Cys642, Ala622, Phe671,

Phe682, Val675, Val743, Leu766, Leu767, Ala769, and Val770, among others (Fig. 2C). These residues further stabilise the ligand binding through hydrophobic interactions. The core backbone of **G1** is located directly above Leu766. The four substituents of the backbone are oriented in different directions and form three hydrogen bond interactions with Asn644, Arg787, and Thr650. In addition, the terminal benzene ring of **G1** forms a π - π stacking interaction with Phe553. This interaction further enhances the binding stability of the ligand to the target protein. These multiple points of contact allow **G1** to penetrate further into the binding pocket and occupy the active site of the enzyme.

2.6 Molecular dynamics (MD) simulation

2.6.1 Analysis on stability. Molecular dynamics simulations are frequently used to explore the interactions between proteins and ligands in dynamic states.³² RMSD can reflect changes in the stability of complex structures. By subjecting compounds **G1** and MGF to 100 ns MD simulations, we assess their binding stability and dynamic behavior within the FASN protein binding site. Fig. 3A and B show the stability of the FASN protein backbone when interacting with compounds **G1** and MGF. The RMSD average of ligand **G1** is 3.91 Å (Fig. 3C). The relatively high value may stem from its flexible movements within the binding site. The RMSD average of ligand MGF is 0.71 Å, indicating a stable structure (Fig. 3D).³³ Overall, neither compound **G1** nor MGF causes significant changes in protein stability upon interaction with FASN.

Table 1 Inhibitory activity and solubility of MGF derivatives

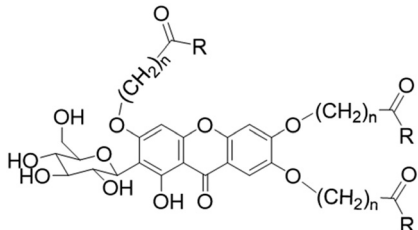
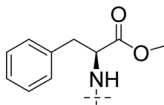
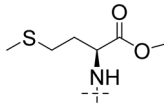
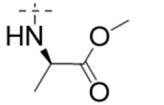
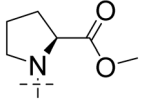
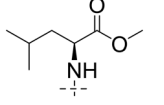
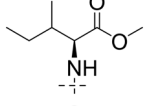
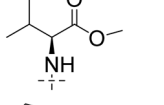
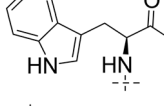
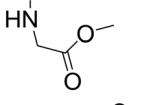
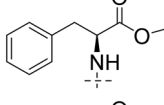
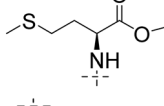
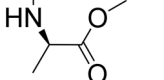
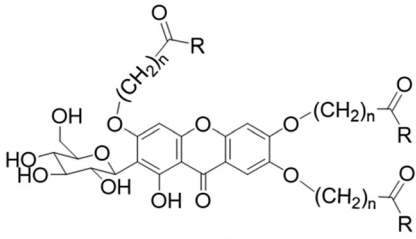
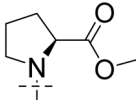
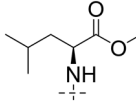
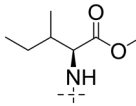
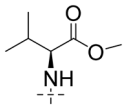
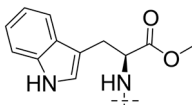
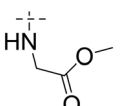
<div></div> G1-G18						
Comp.	<i>n</i>	R	IC ₅₀ (μM)		Equilibrium solubility (mg mL ⁻¹)	log <i>P</i>
			3T3-L1			
G1	4		39.13 ± 0.82		16.29	1.34
G2	4		87.10 ± 2.40		15.23	1.20
G3	4		251.20 ± 4.90		1.40	0.41
G4	4		88.57 ± 1.32		12.79	0.71
G5	4		205.58 ± 2.59		76.64	2.17
G6	4		82.07 ± 1.83		217.55	1.63
G7	4		95.56 ± 1.29		44.52	0.70
G8	4		46.80 ± 1.28		1.25	1.74
G9	4		154.77 ± 2.80		0.59	0.67
G10	5		85.31 ± 3.80		12.20	1.69
G11	5		71.40 ± 1.72		12.97	1.06
G12	5		113.72 ± 2.05		40.30	1.39

Table 1 (continued)

 G1-G18					
Comp.	<i>n</i>	R	IC ₅₀ (μM) 3T3-L1	Equilibrium solubility (mg mL ⁻¹)	log <i>P</i>
G13	5		95.97 ± 1.55	106.39	1.06
G14	5		136.24 ± 1.87	83.87	2.36
G15	5		90.37 ± 3.89	245.75	2.14
G16	5		99.07 ± 1.80	64.41	1.64
G17	5		61.69 ± 1.97	1.31	1.78
G18	5		183.05 ± 3.08	1.35	0.99
MGF			458.99 ± 9.50	0.19	0.02
Orlistat			64.55 ± 2.11		

2.6.2 RMSF analysis. RMSF (root-mean-square fluctuation), a key indicator in dynamics simulations, assesses the mobility of protein residues and ligand atoms. Lower RMSF values signify higher residue stability.³⁴ Fig. 4A and B present RMSF analyses of **G1** and MGF based on protein residues.³⁵ The fluctuation trends of the two simulation systems are similar. Results show that the RMSF value for the **G1** system is 12.19 Å, while the average RMSF value for the MGF system is 14.40 Å. Compared to MGF, the **G1** simulation system exhibits lower overall fluctuation. In summary, the protein-ligand complex maintains a stable conformation throughout the simulation. Compared to MGF, compound **G1** enhances the stability of the entire protein system upon binding.

2.6.3 Analysis on binding free energy. The molecular mechanics and generalised Born surface area (MM-GBSA) method combined with free energy calculations is an important tool for assessing the strength of protein-small molecule interactions.³⁶ Analysis of the data in Fig. 5A and 6A shows that the total energy trajectory fluctuates around the

mean value during the simulation, indicating some stability and equilibrium, and suggesting that the complex reaches equilibrium during the simulation. From Fig. 5B and 6B, the mean total binding free energy of MGF is −34.37 kcal mol^{−1}, while that of **G1** is −66.17 kcal mol^{−1}. As shown in Fig. 5C and 6C, key residues ARG:676 and ASP:788 significantly affect the binding free energy of MGF, whereas LEU:582, VAL:675, PHE:682, and ASP:788 play a decisive role in the binding free energy of **G1**. These findings indicate that compound **G1** exhibits more stable binding interactions with the protein. This may be attributed to **G1**'s longer side chains, which enable deeper penetration into the protein cavity pocket and facilitate the formation of more interactions.

2.7 Effects of compound **G1** on lipid accumulation in 3T3-L1 cells

To study the effect of the compounds on the lipid accumulation in 3T3-L1 cells, the cells were analyzed by oil

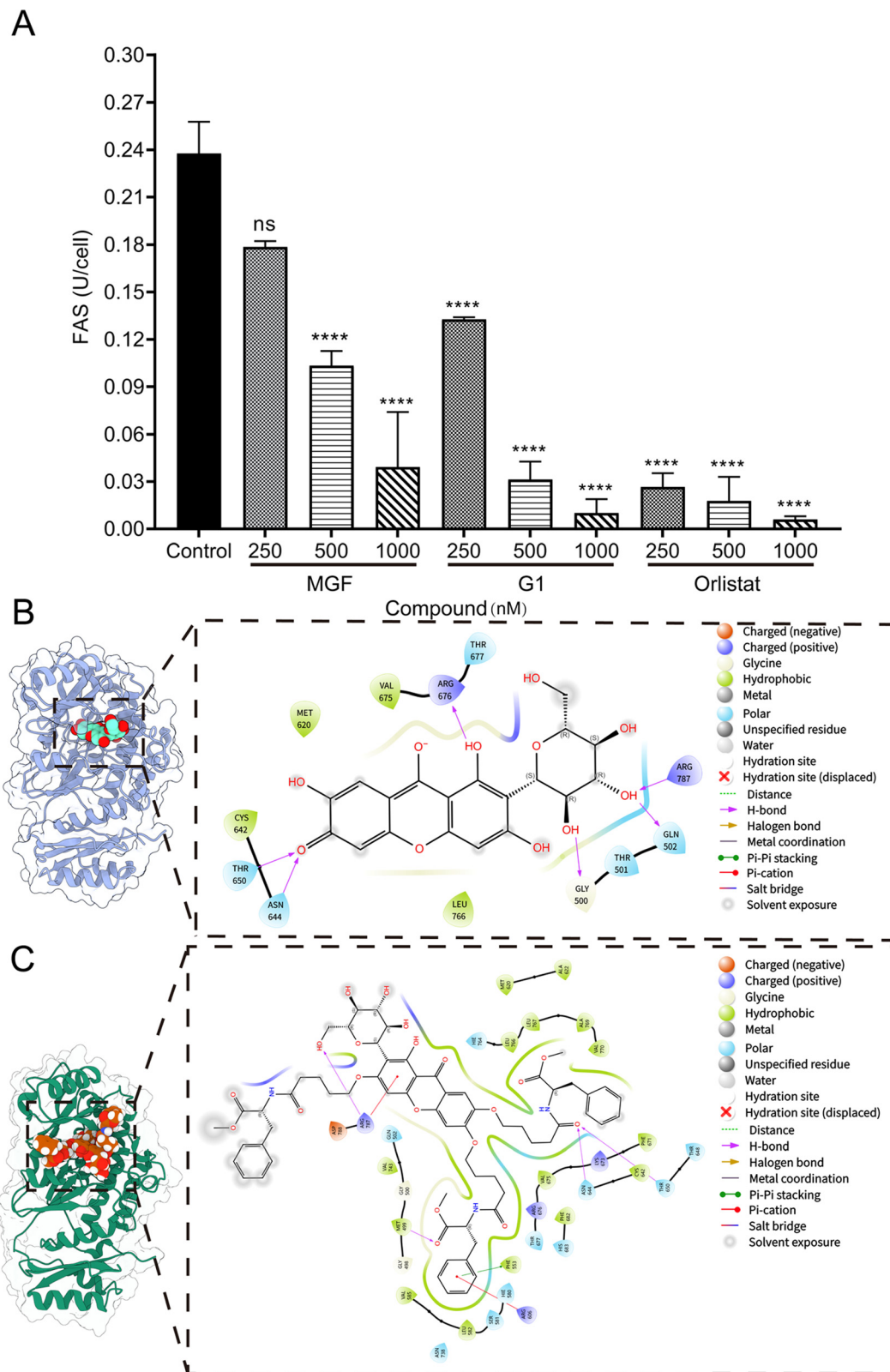


Fig. 2 Inhibitory activity on FASN and docking studies in FASN. (A) The activity of FASN in the presence of MGF and **G1** is shown. The values represent means \pm SD, ($n = 3$), with the control group serving as the reference point. **** $P < 0.001$. (B) MGF and FASN combined model diagrams. (C) **G1** and FASN combined model diagrams.

red O staining on the eighth day of differentiation in treating with **G1** continuously. As illustrated in Fig. 7, the lipid

accumulation in cells with compound **G1** treatment was markedly diminished in a dose-dependent manner in

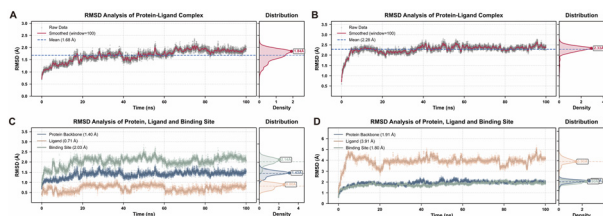


Fig. 3 (A and B) shows the RMSD analysis of protein-ligand complexes in molecular dynamics simulations. X-Axis indicates simulation time (ns), y-axis indicates RMSD value (Å); (C and D) shows the RMSD analysis of the protein backbone, ligand, and binding site, respectively.

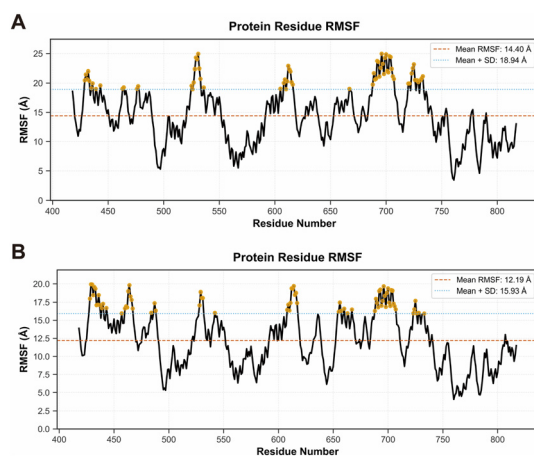


Fig. 4 (A) The RMSF analysis of protein residues and MGF in the molecular dynamics simulations; (B) the RMSF analysis of protein residues and G1 in the molecular dynamics simulations.

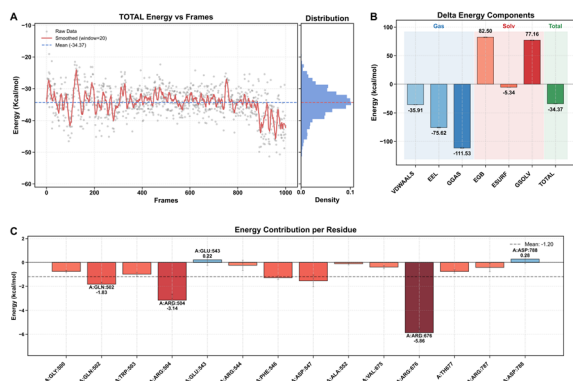


Fig. 5 MM-GBSA binding free energy analysis of complexes formed by MGF with proteins. (A) Variation of total binding energy with the number of simulated frames; (B) histogram of delta energy components; (C) plot of residue energy contribution.

comparison to the control cells, as evidenced by the diminished size and number of lipid droplets.

2.8 Effects of compound G1 on the reactive oxygen species level

During differentiation of 3T3-L1 cells, reactive oxygen species (ROS) accumulation occurs in the adipocytes, and studies have demonstrated that exogenous and endogenous ROS

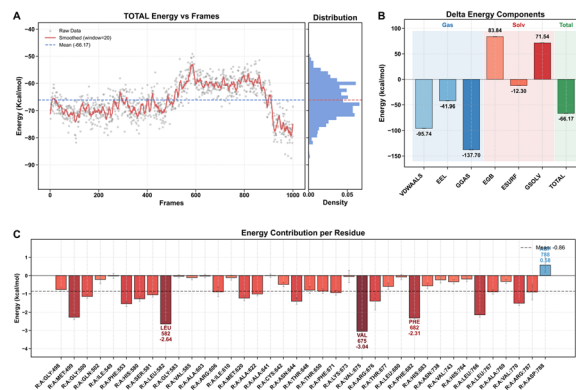


Fig. 6 MM-GBSA binding free energy analysis of complexes formed by G1 with proteins. (A) Variation of total binding energy with the number of simulated frames; (B) histogram of delta energy components; (C) plot of residue energy contribution.

significantly accelerate the differentiation process of adipocytes. As shown in Fig. 8A, the fluorescence of the cells gradually weakened with the increase of compound concentration compared with the model group from microscopic observation. The intracellular ROS level was significantly elevated on the second day of 3T3-L1 cell differentiation in comparison to the control, while the ROS level was significantly diminished by G1 treatment (Fig. 8B and C), indicating that G1 inhibited the differentiation of 3T3-L1 adipocyte cells through the reduction of ROS production.

2.9 Effects of compound G1 on the cell cycle

As a consequence of contact inhibition, undifferentiated 3T3-L1 cells were unable to progress through the cell cycle. Upon the addition of MDI, the normal cell cycle progression was observed. To research the relation between cell growth and cell cycle arrest, 3T3-L1 cells with G1 treatment were subjected to flow cytometry analysis after PI staining. As shown in Fig. 9A and B, approximately 89.4% of normal cells were in the G0/G1 phase, which was reduced to 50.8% in the model group. After treatment of G1, the percentage of cells in

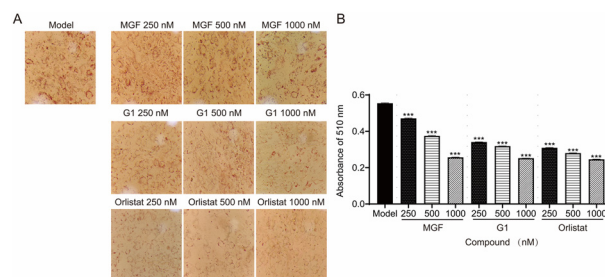


Fig. 7 Inhibition of adipogenesis in 3T3-L1 cells. (A) The lipid accumulation was conducted by measuring oil red O staining. (B) The quantification of stained lipids was conducted by measuring the absorbance at 510 nm. The values represent means \pm SD, ($n = 3$), with the model group serving as the reference point. *** $P < 0.001$.

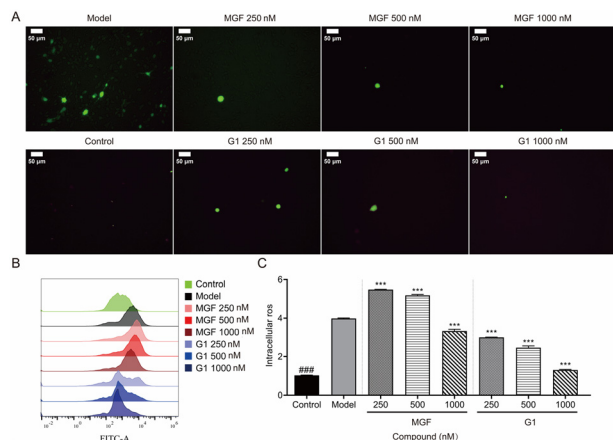


Fig. 8 ROS production. (A) Fluorescence microscopy images indicating intracellular ROS induction. (B) Quantification of ROS by flow cytometry. (C) Quantification of fluorescence intensity in the 3T3-L1 cell line, all data are means \pm SD, ($n = 3$), $###P < 0.001$, $***P < 0.001$ compared with the model group.

the G0/G1 phase increased in a dose-dependent manner from 76.0% to 86.9%. The results indicated that **G1** impeded the cell cycle by inducing arrest in the G0/G1 phase at the onset of adipogenesis.

2.10 Plasma and liver microsomal stability of compound **G1** *in vitro*

Stability of compounds in plasma is an important factor in the drug development process. Therefore, we selected the most active **G1** for plasma stability studies (S56). The results showed that **G1** exhibited moderate plasma stability with $t_{1/2} = 0.38$ h. This metabolic conversion may occur through enzymatic hydrolysis catalyzed by plasma esterases, where the methyl ester group undergoes hydrolytic cleavage due to the inherent susceptibility of ester bonds to enzymatic degradation. In addition, liver microsomes are widely used for *in vitro* evaluation of drug metabolism. Therefore, the most promising compound **G1** was chosen to evaluate the metabolic stability in murine liver microsomes (Table 2). The results showed that **G1** exhibited a comparatively faster metabolic rate with $t_{1/2} = 8.03$ min and $CL_{int} = 0.173$ mL/

min/mg in murine liver microsomes. These findings not only substantiate the foundation for subsequent pharmacokinetic investigations but also offer valuable insights to guide the development of lipophilic drug candidates in future studies.

2.11 Effects of compound **G1** on the body weight, Lee's index, abdominal circumference, organ weight and tissue weight

After 8 weeks of **G1** treatment beginning from the 133rd day, it was clearly observed that **G1** effectively inhibited body weight gain (Fig. 10A). Compared with the HFD group, orlistat, G1-I (30 mg kg^{-1}) and G1-II (60 mg kg^{-1}) groups exhibited a reduction in body weight of 13.44%, 6.81%, and 18.47%, respectively (Fig. 10B). As illustrated in Fig. 10D and E, the abdominal circumference and Lee's index of the mice in the HFD group were markedly elevated in comparison to the NC group, while these trends in the orlistat, G1-I, and G1-II groups were significantly reduced in comparison to the HFD group. Moreover, compared with the NC group, HFD significantly increased the liver weight (Fig. 10C), visceral fat mass (Fig. 10F) and thymus weight (Fig. 10G), while the treatment of **G1** improved these trends, which was consistent with their morphology (Fig. 10H). And the analysis of the above indicators showed that the improvement effect of group G1-II is more obvious than that of group G1-I on body weight and visceral fat mass. Moreover, in comparison with the orlistat group, mice of the G1-II group showed significantly reduced liver weight and visceral fat mass. The results suggested that **G1** effectively inhibited body weight gain and improved body fat levels.

2.12 Effects of compound **G1** on serum lipid levels

It is well established that obesity is frequently accompanied by dyslipidemia. Therefore, we assessed the serum TG, TC, LDL-C and HDL-C levels in order to gain further insight into the effects of compound **G1** on lipid metabolism in an obese mouse model. Effects of compound **G1** on serum lipid levels in HFD obese mice were analyzed. The results showed that the administration of compound **G1** was observed to significantly decrease TG, TC and LDL-C levels, increasing HDL-C levels (Fig. 11A–D). Furthermore, the high-dose group treated with G1-II demonstrated superior efficacy to that of the low-dose group treated with G1-I. In comparison with the orlistat group, mice of the G1-II group showed significantly reduced TG and TC levels. These findings suggest that compound **G1** is capable of ameliorating the dyslipidemia observed in HFD-induced obese mice.

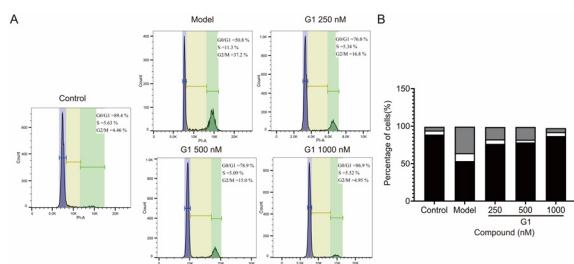


Fig. 9 Cell cycle progression. (A) Flow cytometry. (B) The cell populations at each stage of the cell cycle were analyzed using the FlowJo software.

Table 2 Metabolic stability of **G1** in liver microsomes

Compound	$t_{1/2}$ (min)	CL_{int} (mL/min/mg)
G1	8.03	0.173

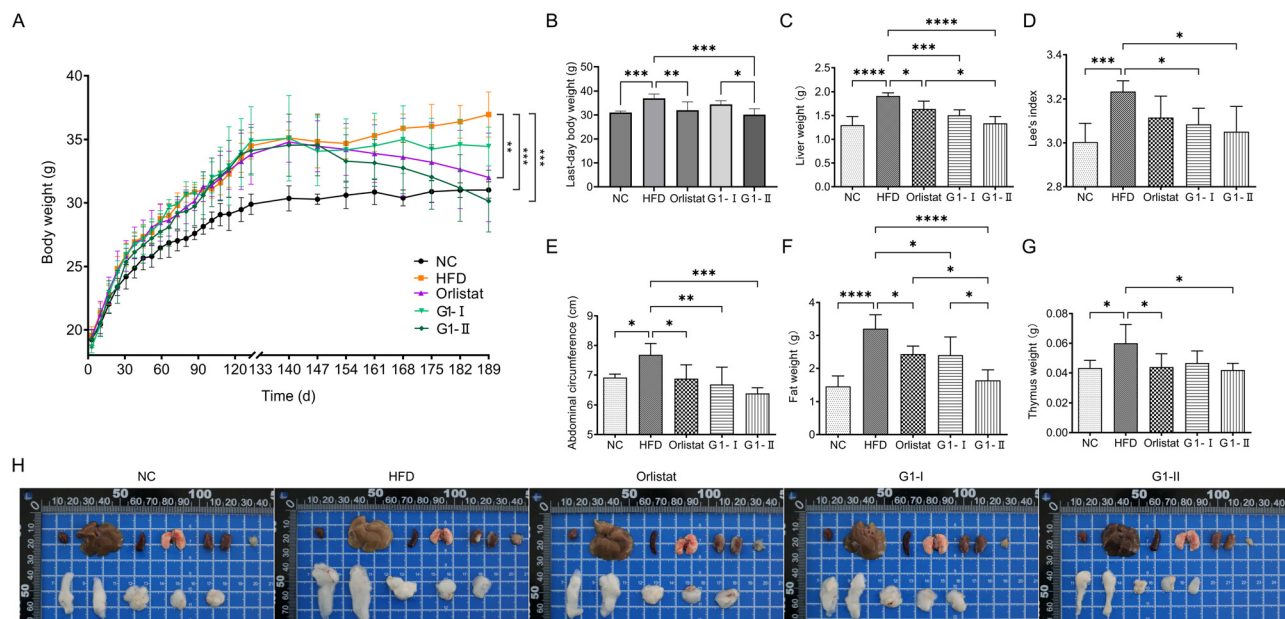


Fig. 10 G1 inhibited body weight gain and improved body fat levels in C57BL/6 mice. (A) Body weight. (B) Body weight at the end of the treatment. (C) Lee's index. (D) Liver weight. (E) Abdominal circumference of mice. (F) Fat weight. (G) Thymus weight. (H) Visceral fat pictures. Values are means \pm SD, ($n = 6$), * $P < 0.05$, ** $P < 0.01$, *** $P < 0.005$, and **** $P < 0.001$.

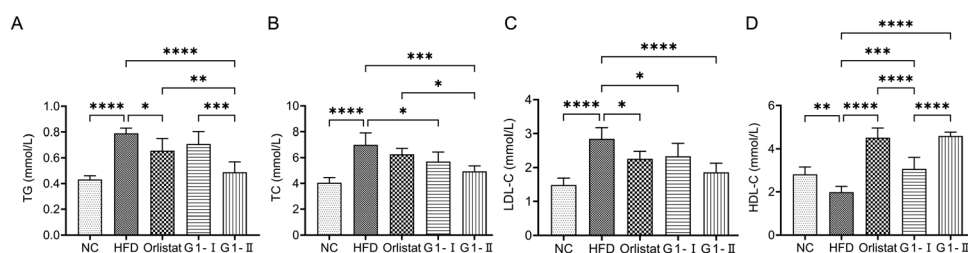


Fig. 11 Serum lipid levels. (A) TG in serum. (B) TC in serum. (C) LDL-C in serum. (D) HDL-C in serum. The values represent means \pm SD, ($n = 6$). The statistical significance levels are as follows: * $P < 0.05$, ** $P < 0.01$, *** $P < 0.005$, and **** $P < 0.001$.

2.13 Effects of compound G1 on fat accumulation and organ damage *in vivo*

The results of oil red O staining of visceral tissues revealed that the liver, kidney, intestinal and epididymal tissues of the HFD group exhibited a considerable number of fat droplets (Fig. 12). G1 treatment significantly reduced lipid accumulation in visceral tissues in a dose-dependent manner. Notably, therapeutic efficacy profiling revealed that group G1-II demonstrated statistically superior outcomes *versus* group G1-I. To study the effect of G1 on organ damage, the HE staining of heart, liver, spleen, lung, and kidney tissues was analyzed (Fig. 13). The results demonstrated that the hepatocytes of the NC group were neatly arranged with a clear cellular morphology. Compared with the NC group, the liver cells in the HFD group exhibited notable steatosis, characterized by an abundance of lipid droplets within the cytoplasm and interstitial space, an increase in cell volume, and a dispersed cellular distribution while the treatment of G1 improved these trends in comparison to the HFD group.

Similarly, the morphology of spleen, lung, and kidney tissues was significantly improved in G1-treated mice. These results validated the effectiveness of G1 on inhibiting fat accumulation without causing apparent toxicity *in vivo*.

3. Conclusions

In conclusion, the discovery and optimization of novel MGF derivatives was carried out for the purpose of increasing lipophilicity and enhancing the anti-obesity effect. Compound G1 exhibited high lipophilicity and good cell inhibitory activity. It triggered the G0/G1 phase cell cycle arrest and the production of intracellular ROS in a concentration-dependent manner in 3T3-L1 cells. The intraperitoneal administration of G1 significantly inhibited body, organ and tissue weight gain, reduced lipid dysfunction, and ameliorated pathological characteristics in high-fat diet induced C57BL/6J obese mice. Furthermore, G1 was found to increase inhibitory activity on FASN. Overall, G1 showed its potential as a lipid regulating agent derived from

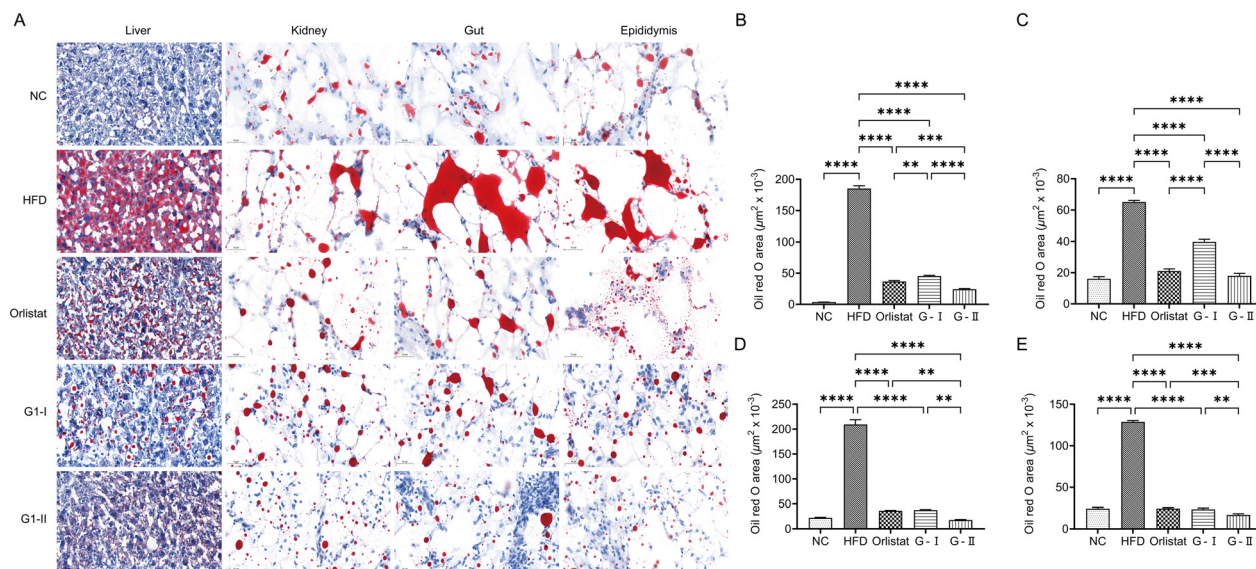


Fig. 12 Effect of G1 on fat accumulation in organs. (A) Micrographs of organ sections stained with oil red O. Lipid droplet area after oil red O staining of liver tissue (B), kidney tissue (C), intestinal tissue (D) and epididymal tissue (E). Values are means \pm SD, ($n = 3$), ** $P < 0.01$, *** $P < 0.005$, and **** $P < 0.001$.

a natural product for the treatment of obesity and deserves to be further explored.

4. Experimental

All solvents were of reagent grade or HPLC grade. Unless otherwise specified, all materials were from commercial suppliers. All the reactions were monitored by thin-layer chromatography using commercial silica gel GF₂₅₄ plates. Chromatographic purification was conducted on a commercial silica gel column (200–300 meshes, Qingdao Haiyang Chemical Co., Ltd., China). ¹H (600 MHz) and ¹³C (150 MHz) nuclear magnetic resonance (NMR) spectra were measured on a JNM-ECP 600 MHz instrument (JEOL Ltd., Japan). Solutions were prepared in deuterated DMSO with chemical shifts (δ) which are given in ppm referenced to deuterated solvent as an internal standard. High-resolution ESI mass spectrometry (HRESIMS) data were acquired on an Orbitrap Exploris 120 mass instrument (Thermo Fisher Scientific, America). The derivatives were of >95% purity as

analyzed by HPLC (LC-20AD, Shimadzu, Japan) equipped with a Shimadzu SPD-M20A UV-vis detector operated at a wavelength of 258 nm using an Agilent reversed phase C18 column (250 mm \times 4.6 mm, 5 μm).

4.1 General procedure for the synthesis of intermediates A1–A18

Amino acid methyl ester hydrochloride (1.00 g, 1.0 eq.) and triethylamine (5.0 eq.) were dissolved in pre-dried dichloromethane. Then, a solution of 5-bromovaleryl chloride or 6-bromohexanoyl chloride (1.0 eq.) in pre-dried dichloromethane was added dropwise at 0 °C. The reaction mixture was stirred for 3–6 h at room temperature. The mixture was washed with water ($\times 3$) and brine ($\times 3$), respectively. The organic layers were dried over Na₂SO₄ and concentrated *in vacuo*. The residue was purified by silica gel column chromatography to get intermediates A1–A18.

4.1.1 5-Bromopentanoyl L-phenylalanine methyl ester (A1). White solid. Yield: 1.21 g (76.1%). ¹H NMR (600 MHz, DMSO-*d*₆), δ 8.31 (1H, d, $J = 7.9$ Hz, NH), 7.29–7.18 (5H, m, the benzene ring), 4.53–4.45 (1H, m, NH-CH), 3.60 (3H, s, CH₃), 3.45 (2H, t, $J = 6.7$ Hz, Br-CH₂), 3.04 (1H, dd, $J = 13.9, 5.2$ Hz, ph-CH₂), 2.88 (1H, dd, $J = 13.7, 9.9$ Hz, ph-CH₂), 2.09 (2H, ddd, $J = 9.6, 6.3, 2.2$ Hz, CH₂), 1.65 (2H, p, $J = 6.5$ Hz, CH₂), 1.53 (2H, p, $J = 7.3$ Hz, CH₂). ¹³C NMR (150 MHz, DMSO-*d*₆), δ 172.2 (C=O), 172.1 (C=O). The benzene ring [137.3, 129.0, 128.2, 126.5], 53.4 (CH), 51.8 (OCH₃), 36.7 (CH₂), 34.8 (CH₂), 31.9 (CH₂), 26.9 (CH₂), 24.2 (CH₂).

4.1.2 5-Bromopentanoyl L-methionine methyl ester (A2). White solid. Yield: 1.24 g (76.1%). ¹H NMR (600 MHz, DMSO-*d*₆), δ 8.25 (1H, d, $J = 7.6$ Hz, NH), 4.35 (1H, quin, CH), 3.61 (3H, s, OCH₃), 3.52 (2H, t, $J = 6.7$ Hz, Br-CH₂), 2.46 (2H, m,

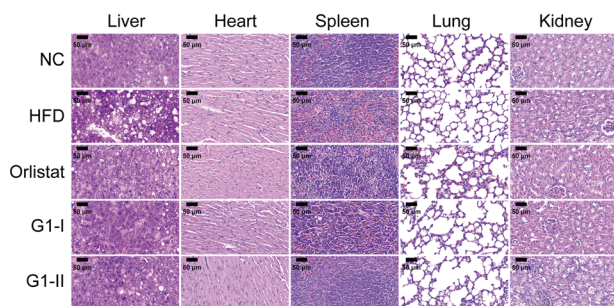


Fig. 13 Micrographs of HE stained sections of organs.

S-CH₂), 2.15 (2H, quin, $J = 7.3$ Hz, CH₂), 2.03 (3H, s, S-CH₃), 1.88 (2H, m, CO-CH₂), 1.78 (2H, m, CH₂), 1.60 (2H, m, CH₂). ¹³C NMR (150 MHz, DMSO-*d*₆), δ 172.4 (C=O), 172.2 (C=O), 51.9 (O-CH₃), 50.8 (NH-CH), 34.7 (CO-CH₂), 33.9 (Br-CH₂), 31.6 (CH₂), 30.4 (CH₂), 29.6 (CH₂), 23.8 (CH₂), 14.6 (S-CH₃).

4.1.3 5-Bromopentanoyl L-alanine methyl ester (A3). White solid. Yield: 1.49 g (78.0%). ¹H NMR (600 MHz, DMSO-*d*₆), δ 8.27 (1H, d, $J = 7.0$ Hz, NH), 4.24 (1H, quin, CH), 3.60 (3H, s, CH₃), 3.52 (2H, t, $J = 6.8$ Hz, CH₂), 2.13 (2H, t, $J = 1.9$ Hz, CH₂), 1.78 (2H, m, CH₂), 1.60 (2H, m, CH₂), 1.25 (3H, d, $J = 7.3$ Hz, CH₃). ¹³C NMR (150 MHz, DMSO-*d*₆), δ 173.2 (C=O), 171.8 (C=O), 51.8 (O-CH₃), 47.5 (NH-CH), 34.8 (Br-CH₂), 33.8 (CO-CH₂), 31.6 (CH₂), 23.8 (CH₂), 16.9 (CH₃).

4.1.4 5-Bromopentanoyl L-proline methyl ester (A4). White solid. Yield: 0.98 g (55.7%). ¹H NMR (600 MHz, DMSO-*d*₆), δ 4.27 (1H, t, $J = 8.8, 4.4, 1.7$ Hz, N-CH), 3.60 (3H, s, OCH₃), 3.56–3.47 (4H, m, CH₂), 2.28–2.11 (2H, m, CH₂), 1.94–1.88 (2H, m, CH₂), 1.84–1.67 (4H, m, CH₂), 1.53–1.48 (2H, m, CH₂), 1.43–1.36 (2H, m, CH₂). ¹³C NMR (150 MHz, DMSO), δ 172.6 (C=O), 170.4 (C=O), 58.1 (N-CH), 51.7 (OCH₃), 46.5 (N-CH₂), 34.9 (CH₂), 31.7 (CH₂), 31.5 (CH₂), 28.8 (CH₂), 28.7 (CH₂), 24.4 (CH₂), 24.4 (CH₂).

4.1.5 5-Bromopentanoyl L-leucine methyl ester (A5). White solid. Yield: 1.46 g (85.9%). ¹H NMR (600 MHz, DMSO-*d*₆), δ 8.20 (1H, s, NH), 4.27 (1H, t, CH-NH), 3.61 (3H, s, OCH₃), 3.52 (2H, t, CH₂), 2.15 (2H, q, CH₂), 1.82–1.74 (2H, m, CH₂), 1.65–1.60 (2H, m, CH₂), 1.60–1.55 (1H, m, CH), 1.55–1.42 (2H, m, CH₂), 0.90–0.82 (6H, m, CH₃). ¹³C NMR (150 MHz, DMSO), δ 173.1 (C=O), 172.0 (C=O), 51.7 (CH), 50.1 (OCH₃), 33.8 (CH₂), 31.6 (CH₂), 24.2 (CH₂), 23.8 (CH), 22.7 (CH₂), 21.2 (CH₃), 21.1 (CH₃).

4.1.6 5-Bromopentanoyl L-isoleucine methyl ester (A6). White solid. Yield: 1.19 g (70.0%). ¹H NMR (600 MHz, DMSO-*d*₆), δ 8.12 (1H, dd, $J = 8.2, 2.1$ Hz, NH), 4.21 (1H, dd, $J = 8.1, 6.6$ Hz, NH-CH), 3.62 (3H, s, OCH₃), 3.52 (2H, td, $J = 6.7, 2.3$ Hz, CH₂), 2.19 (2H, td, $J = 7.2, 3.5$ Hz, CH₂), 1.81–1.73 (3H, m, CH, CH₂), 1.60 (2H, p, $J = 7.4$ Hz, CH₂), [1.43–1.34 (1H, m, CH₂), 1.22–1.15 (1H, m, CH₂)], 0.83 (6H, m, CH₃ × 2). ¹³C NMR (150 MHz, DMSO), δ 172.2 (C=O), 172.2 (C=O), 56.3 (CH), 51.5 (CH₃), 36.2 (CH-CH₃), 34.7 (CH₂), 33.7 (CH₂), 31.6 (CH₂), 24.8 (CH₂), 23.9 (CH₂), 15.4 (CH₃), 11.0 (CH₃).

4.1.7 5-Bromopentanoyl L-valine methyl ester (A7). White solid. Yield: 1.30 g (74.3%). ¹H NMR (600 MHz, DMSO-*d*₆), δ 8.11 (1H, d, $J = 8.1$ Hz, NH), 4.16 (1H, dd, $J = 8.1, 6.4$ Hz, CH), 3.62 (3H, s, OCH₃), 3.53 (2H, t, Br-CH₂), 2.20 (2H, m, CH₂), 2.01 (1H, m, $J = 6.9$ Hz, CH), 1.77 (2H, m, CH₂), 1.61 (2H, m, CH₂), 0.87 (6H, dd, $J = 11.4, 6.8$ Hz, CH₃ × 2). ¹³C NMR (150 MHz, DMSO), δ 172.3 (C=O), 172.2 (C=O), 57.3 (NH-CH), 51.6 (OCH₃), 34.7 (CH₂), 33.7 (CH₂), 31.6 (CH), 29.8 (CH₂), 23.9 (CH₂), 19.0 (CH₃), 18.3 (CH₃).

4.1.8 5-Bromopentanoyl L-tryptophan methyl ester (A8). White solid. Yield: 1.18 g (78.8%). ¹H NMR (600 MHz, DMSO-*d*₆), δ 10.86 (1H, d, NH), 8.28 (1H, d, $J = 7.6$ Hz, NH). The benzene ring [7.49 (1H, d, $J = 7.8$ Hz), 7.34 (1H, d, $J = 8.1$ Hz), 7.06 (1H, t), 6.98 (1H, t, $J = 7.4$ Hz)], 7.15 (1H, d, $J = 2.4$ Hz, NH-CH), 4.51 (1H, quin, $J = 8.3, 5.6$ Hz, NH-CH), 3.58 (3H, s,

OCH₃), 3.46 (1H, t, $J = 6.7$ Hz, Br-CH₂), 3.09 (2H, m, CH-CH₂), 2.12 (2H, m, CO-CH₂), 1.66 (2H, m, CH₂), 1.54 (2H, m, CH₂). ¹³C NMR (150 MHz, DMSO-*d*₆), δ 172.6 (C=O), 171.9 (C=O). The benzene ring [136.1, 127.1, 121.0, 118.4, 118.0, 111.4], 123.7 (C=CH), 109.6 (C-CH₂), 53.0 (OCH₃), 51.8 (NH-CH), 34.8 (Br-CH₂), 33.8 (CO-CH₂), 31.4 (CH₂), 27.1 (CH₂), 23.7 (CH₂).

4.1.9 5-Bromopentanoyl L-glycine methyl ester (A9). White solid. Yield: 1.51 g (75.1%). ¹H NMR (600 MHz, DMSO-*d*₆), δ 8.31 (1H, d, $J = 17.9$ Hz, NH), 3.85–3.76 (2H, m, CH₂), 3.76–3.65 (3H, m, OCH₃), 3.16–3.09 (2H, m, CH₂), 2.38–2.18 (2H, m, CH₂), 1.67–1.41 (4H, m, CH₂ × 2). ¹³C NMR (151 MHz, DMSO), δ 172.4 (C=O), 170.5 (C=O), 51.6 (OCH₃), 40.5 (CH₂), 34.8 (CH₂), 33.9 (CH₂), 31.6 (CH₂), 23.8 (CH₂).

4.1.10 6-Bromohexanoyl L-phenylalanine methyl ester (A10). White solid. Yield: 1.46 g (88.5%). ¹H NMR (600 MHz, DMSO-*d*₆), δ 8.27 (1H, d, $J = 7.9$ Hz, NH), 7.29–7.19 (5H, m, the benzene ring), 4.49 (1H, ddd, $J = 10.1, 7.9, 5.3$ Hz, NH-CH), 3.45 (2H, t, $J = 6.7$ Hz, Br-CH₂), 3.03 (1H, dd, $J = 13.8, 5.4$ Hz, ph-CH₂), 2.88 (1H, dd, $J = 13.8, 9.7$ Hz, ph-CH₂), 2.10–2.01 (2H, m, CH₂), 1.77–1.69 (2H, m, CH₂), 1.46–1.37 (2H, m, CH₂), 1.29–1.19 (2H, m, CH₂). ¹³C NMR (150 MHz, DMSO), δ 172.2 (C=O), 172.1 (C=O). The benzene ring [137.3, 129.0, 128.2, 126.5], 53.4 (CH), 51.8 (OCH₃), 39.5 (CH₂), 36.7 (CH₂), 34.9 (CH₂), 34.7 (CH₂), 32.0 (CH₂), 27.0 (CH₂), 24.2 (CH₂).

4.1.11 6-Bromohexanoyl L-methionine methyl ester (A11). White solid. Yield: 1.31 g (77.1%). ¹H NMR (600 MHz, DMSO-*d*₆), δ 8.27 (1H, d, $J = 7.6$ Hz, NH), 4.39 (1H, quin, CH), 3.66 (3H, s, OCH₃), 3.55 (2H, t, $J = 6.8$ Hz, Br-CH₂), 2.54 (2H, t, $J = 2.3$ Hz, S-CH₂), 2.16 (2H, quin, $J = 7.2$ Hz, CH₂), 2.07 (3H, s, S-CH₃), 1.93 (2H, m, CO-CH₂), 1.83 (2H, m, CH₂), 1.55 (2H, m, CH₂), 1.39 (2H, m, CH₂). ¹³C NMR (150 MHz, DMSO-*d*₆), δ 172.4 (C=O), 172.3 (C=O), 51.9 (O-CH₃), 50.8 (NH-CH), 35.0 (CO-CH₂), 34.7 (Br-CH₂), 32.0 (CH₂), 30.5 (CH₂), 29.6 (CH₂), 27.1 (CH₂), 24.3 (CH₂), 14.5 (S-CH₃).

4.1.12 6-Bromohexanoyl L-alanine methyl ester (A12). White solid. Yield: 1.57 g (78.1%). ¹H NMR (600 MHz, DMSO-*d*₆), δ 8.22 (1H, d, $J = 6.9$ Hz, NH), 4.24 (1H, quin, $J = 7.3$ Hz, CH), 3.61 (3H, s, CH₃), 3.51 (2H, t, $J = 6.7$ Hz, CH₂), 2.10 (2H, t, $J = 7.4$ Hz, CH₂), 1.79 (2H, m, CH₂), 1.50 (3H, m, CH₂), 1.36 (2H, m, CH₂), 1.25 (3H, d, $J = 7.3$ Hz, CH₃). ¹³C NMR (150 MHz, DMSO-*d*₆), δ 173.3 (C=O), 172.0 (C=O), 51.8 (O-CH₃), 47.4 (NH-CH), 35.0 (CO-CH₂), 34.7 (Br-CH₂), 32.0 (CH₂), 27.1 (CH₂), 24.3 (CH₂), 17.0 (CH₃).

4.1.13 6-Bromohexanoyl L-proline methyl ester (A13). White solid. Yield: 1.26 g (68.1%). ¹H NMR (600 MHz, DMSO-*d*₆), δ 4.26 (1H, t, CH-CO), 3.60 (3H, s, OCH₃), 3.56–3.49 (4H, m, CH₂), 2.27 (1H, m, CH₂), 2.14 (1H, m, CH₂), 2.07–1.94 (1H, m, CH₂), 1.90 (2H, p, $J = 6.9$ Hz, CH₂), 1.81 (2H, m, CH₂), 1.73 (1H, m, CH₂), 1.59 (2H, m, CH₂). ¹³C NMR (150 MHz, DMSO), δ 172.6 (C=O), 170.6 (C=O), 58.2 (C-CO), 51.6 (O-CH₃), 46.5 (N-CH₂), 33.2 (CH₂), 32.1 (CH₂), 28.8 (CH₂), 27.3 (CH₂), 24.4 (CH₂), 23.4 (CH₂).

4.1.14 6-Bromohexanoyl L-leucine methyl ester (A14). White solid. Yield: 1.60 g (90.4%). ¹H NMR (600 MHz, DMSO-*d*₆), δ 8.16 (1H, s, NH), 4.28 (1H, t, NH-CH), 3.61 (3H, s,

OCH₃), 3.49 (2H, t, Br-CH₂), 2.12 (2H, td, *J* = 7.3, 3.1 Hz, CO-CH₂), 1.79 (2H, p, *J* = 6.8 Hz, CH₂), 1.65–1.54 (2H, m, CH₂), 1.53–1.48 (2H, m, CH₂), 1.45 (1H, td, *J* = 9.0, 4.5 Hz, CH), 1.38–1.34 (2H, m, CH₂), 0.88 (3H, d, *J* = 6.7 Hz, CH₃), 0.83 (3H, d, *J* = 6.6 Hz, CH₃). ¹³C NMR (150 MHz, DMSO), δ 173.1 (C=O), 172.2 (C=O), 51.7 (NH-CH), 50.1 (OCH₃), 34.8 (CH₂), 31.9 (CH₂), 27.1 (CH₂), 24.3 (CH₂), 22.7 (CH₂), 22.7 (CH), 21.2 (CH₃), 21.1 (CH₃).

4.1.15 6-Bromohexanoyl L-isoleucine methyl ester (A15). White solid. Yield: 1.52 g (85.8%). ¹H NMR (600 MHz, DMSO-*d*₆), δ 8.10 (1H, s, NH), 4.21 (1H, dd, *J* = 7.5, 6.7, 1.5 Hz, NH-CH), 3.61 (3H, s, OCH₃), 3.50 (2H, t, CH₂), 2.15 (2H, t, CH₂), 1.82–1.76 (2H, m, CH₂), 1.54–1.48 (2H, m, CH₂), 1.28 (4H, m, CH₂ × 2), 0.82 (6H, m, CH₃ × 2). ¹³C NMR (150 MHz, DMSO), δ 172.3 (C=O), 172.3 (C=O), 56.2 (CH), 51.5 (CH₃), 36.2 (CH-CH₃), 35.0 (CH₂), 34.6 (CH₂), 31.9 (CH₂), 27.1 (CH₂), 24.8 (CH₂), 24.4 (CH₂), 15.4 (CH₃), 11.0 (CH₃).

4.1.16 6-Bromohexanoyl L-valine methyl ester (A16). White solid. Yield: 1.49 g (80.9%). ¹H NMR (600 MHz, DMSO), δ 8.10 (1H, s, NH), 4.20 (1H, d, NH-CH), 3.61 (3H, s, CH₃), 3.50 (2H, t, CH₂), 2.15 (1H, m, CH), 1.76 (2H, t, CH₂), 1.50 (2H, m, CH₂), 1.35 (2H, m, CH₂), 1.30 (2H, m, CH₂), 0.82 (6H, m, CH₃). ¹³C NMR (150 MHz, DMSO), δ 172.3 (C=O), 172.3 (C=O), 56.2 (NH-CH), 51.5 (OCH₃), 36.2 (CO-CH₂), 34.6 (CH₂), 32.0 (CH₂), 27.1 (CH₂), 24.8 (CH₂), 24.4 (CH₂), 15.4 (CH₃), 11.0 (CH₃).

4.1.17 6-Bromohexanoyl L-tryptophan methyl ester (A17). White solid. Yield: 1.45 g (93.5%). ¹H NMR (600 MHz, DMSO-*d*₆), δ 10.86 (1H, d, *J* = 2.6 Hz, NH), 8.24 (1H, d, *J* = 7.7 Hz, NH). The benzene ring [δ 7.50 (1H, d, *J* = 7.8 Hz), 7.34 (1H, d, *J* = 8.1 Hz), 7.07 (1H, d, *J* = 2.4 Hz), 6.99 (1H, t, *J* = 7.4 Hz)], 7.14 (1H, m, NH-CH), 4.53 (1H, td, *J* = 8.1, 5.5 Hz, CO-CH), 3.59 (3H, s, OCH₃), 3.45 (2H, t, *J* = 6.7 Hz, Br-CH₂), 3.09 (2H, m, CH₂), 2.09 (2H, m, CO-CH₂), 1.74 (2H, m, CH₂), 1.44 (2H, m, CH₂), 1.27 (2H, m, *J* = 9.5, 6.4 Hz, CH₂). ¹³C NMR (150 MHz, DMSO-*d*₆), δ 172.6 (C=O), 172.1 (C=O), The benzene ring [136.1, 127.1, 120.9, 118.4, 118.0, 111.4], 123.6 (C=CH), 109.6 (C=CH), 53.0 (OCH₃), 51.8 (NH-CH), 34.9 (Br-CH₂), 34.8 (CO-CH₂), 32.0 (CH₂), 27.1 (CH₂), 27.0 (CH₂), 24.2 (CH₂).

4.1.18 6-Bromohexanoyl L-glycine methyl ester (A18). White solid. Yield: 1.53 g (72.2%). ¹H NMR (600 MHz, DMSO-*d*₆), δ 8.25 (1H, t, *J* = 11.5, 8.7 Hz, NH), 3.80 (2H, d, *J* = 5.7 Hz, NH-CH₂), 3.61 (3H, s, OCH₃), 3.51 (2H, t, *J* = 13.5 Hz, CH₂), 2.12 (2H, t, CH₂), 1.79 (2H, m, CH₂), 1.51 (2H, m, CH₂), 1.37 (2H, m, CH₂). ¹³C NMR (150 MHz, DMSO), δ 172.6 (C=O), 170.5 (C=O), 51.6 (OCH₃), 40.5 (NH-CH₂), 35.0 (CH₂), 34.8 (CH₂), 32.0 (CH₂), 27.1 (CH₂), 24.3 (CH₂).

4.2 General procedure for the synthesis of the target compounds G1–G18

MGF (0.30 g, 1.0 eq.) and K₂CO₃ (5.0 eq.) were added to a solution of the intermediates (A1–A18; 5.0 eq.) in DMF at 80 °C under N₂ protection. The mixture was then kept stirring for 12–18 h at 80 °C. And upon completion, the reaction mixture was filtered and concentrated *in vacuo*.

The residue was purified by silica gel column chromatography to obtain the target compounds G1–G18.

4.2.1 5-(1-Hydroxy-2-((3*R*,4*R*,5*S*,6*R*)-3,4,5-trihydroxy-6-(hydroxymethyl) tetrahydro-2*H*-pyran-2-yl)-9*H*-xanthen-9-one-3,6,7-triyl) pentanoyl L-phenylalanine methyl ester (G1). Yellow amorphous powder. Yield: 0.26 g (30.2%). ¹H NMR (600 MHz, DMSO-*d*₆), δ 13.58 (1H, s, OH), 8.33 (3H, d, *J* = 13.8, 7.8 Hz, NH × 3), 7.47 (1H, s, H-8), 7.32–7.19 (15H, m, CH × 15), 7.15 (1H, s, H-5), 6.60 (1H, s, H-4), 4.88 (1H, s, H-1'), 4.63 (2H, s, OH × 2), 4.50 (3H, d, CH × 3), 4.43 (1H, s, OH), 4.16–3.88 (8H, m, CH₂ × 3, CH, OH), 3.60 (12H, d, *J* = 6.1 Hz, CH₃ × 3, CH × 3), 3.35 (2H, s, CH₂), [3.04 (d, 3H), 2.89 (d, 3H), CH₂ × 3], 2.15 (6H, m, CH₂ × 3), 1.69–1.55 (12H, m, CH₂ × 6). ¹³C NMR (150 MHz, DMSO), δ 179.1 (C-9), 172.3 (C=O × 3), 172.1 (C=O × 3), 164.9 (C-3), 160.5 (C-1), 156.8 (C-4a), 155.4 (C-6), 151.8 (C-4b), 146.2 (C-7), 137.3 (C-1' × 3), 129.0 (C-3' × 3, C-5' × 3), 128.2 (C-2' × 3, C-6' × 3), 126.5 (C-4' × 3), 112.2 (C-8a), 109.0 (C-8), 105.4 (C-2), 102.5 (C-5), 101.9 (C-9a), 91.0 (C-4), 81.8 (C-1'), 79.1 (C-5'), 72.5 (C-2'), 71.0 (C-3'), 70.4 (C-4'), 68.7 (CH₂), 68.4 (CH₂), 68.2 (CH₂), 62.0 (C-6'), 53.4 (N-CH × 3), 51.8 (O-CH₃ × 3), 36.7 (CH₂ × 3), 34.3 (CH₂ × 3), 27.6 (CH₂ × 3), 21.6 (CH₂ × 3). HRESIMS *m/z* 1228.4827 [M + Na]⁺ (calcd for C₆₄H₇₅O₂₀N₃Na, 1228.4836).

4.2.2 5-(1-Hydroxy-2-((3*R*,4*R*,5*S*,6*R*)-3,4,5-trihydroxy-6-(hydroxymethyl) tetrahydro-2*H*-pyran-2-yl)-9*H*-xanthen-9-one-3,6,7-triyl) pentanoyl L-methionine methyl ester (G2). Yellow amorphous powder. Yield: 0.20 g (24.4%). ¹H NMR (600 MHz, DMSO-*d*₆), δ 13.55 (1H, s, OH-1), 8.27 (6H, d, NH), 7.48 (1H, s, H-8), 7.16 (1H, s, H-5), 6.60 (1H, s, H-4), 3.34–4.86 (OH, NCH, OCH₃ and OCH₂), 1.69–2.50 (SCH₃, SCH₂ and CH₂). ¹³C NMR (150 MHz, DMSO-*d*₆), δ 179.1 (C-9), 172.5 (C=O × 6), 164.9 (C-3), 160.4 (C-1), 156.9 (C-4a), 155.5 (C-6), 151.8 (C-4b), 146.2 (C-7), 112.2 (C-8a), 109.0 (C-8), 105.5 (C-2), 102.0 (C-5), 100.8 (C-8b), 91.0 (C-4), 81.8 (C-1'), 79.0 (C-5'), 72.5 (C-2'), 71.0 (C-3'), 70.4 (C-4'), 68.7 (OCH₂), 68.3 (OCH₂), 68.0 (OCH₂), 62.0 (C-6'), 51.9 (NCH), 51.9 (NCH), 51.9 (NCH), 50.9 (O-CH₃), 50.9 (O-CH₃), 50.9 (O-CH₃), 34.5 (CO-CH₂), 34.5 (CO-CH₂), 34.4 (CO-CH₂), 30.5 (CH₂), 30.5 (CH₂), 30.5 (CH₂), 29.6 (CH₂), 29.6 (CH₂), 29.6 (CH₂), 27.9 (CH₂), 27.9 (CH₂), 27.7 (CH₂), 21.7 (CH₂), 21.7 (CH₂), 21.7 (CH₂), 14.6 (CH₃), 14.6 (CH₃), 14.6 (CH₃). HRESIMS *m/z* 1158.4169 [M + H]⁺ (calcd for C₅₂H₇₆N₃O₂₀S₃, 1158.4179).

4.2.3 5-(1-Hydroxy-2-((3*R*,4*R*,5*S*,6*R*)-3,4,5-trihydroxy-6-(hydroxymethyl) tetrahydro-2*H*-pyran-2-yl)-9*H*-xanthen-9-one-3,6,7-triyl) pentanoyl L-alanine methyl ester (G3). Yellow amorphous powder. Yield: 0.23 g (32.9%). ¹H NMR (600 MHz, DMSO-*d*₆), δ 13.56 (1H, s, OH-1), 8.27 (3H, d, *J* = 6.8 Hz, NH × 3), 7.47 (1H, s, H-8), 7.16 (1H, s, H-5), 6.61 (1H, s, H-4), 3.36–4.86 (OH, OCH₃, OCH₂ and CH), 2.21 (6H, m, CO-CH₂), 1.78 (6H, m, CH₂ × 3), 1.69 (6H, m, CH₂ × 3), 1.27 (9H, m, CH₃ × 3). ¹³C NMR (150 MHz, DMSO-*d*₆), δ 179.1 (C-9), 173.3 (NH-CO), 172.1 (CO-CH), 164.9 (C-3), 160.4 (C-1), 155.5 (C-6), 151.8 (C-10a), 146.2 (C-7), 112.2 (C-8a), 109.0 (C-8), 105.5 (C-2), 101.9 (C-5), 100.8 (C-9a), 91.0 (C-4), 81.9 (C-1'), 79.0 (C-5'), 72.5 (C-2'), 71.0 (C-3'), 70.4 (C-4'), 68.8 (OCH₂), 68.4 (OCH₂), 68.1 (OCH₂), 62.0 (C-6'), 51.8 (NCH × 3), 34.4 (CO-CH₂),

34.4 (CO-CH₂), 34.4 (CO-CH₂), 27.9 (CH₂), 27.8 (CH₂), 27.7 (CH₂), 21.7 (CH₂ × 3), 16.9 (CH₃ × 3). HRESIMS *m/z* 978.4075 [M + H]⁺ (calcd for C₄₆H₇₀N₃O₂₀, 978.4078).

4.2.4 5-(1-Hydroxy-2-((3*R*,4*R*,5*S*,6*R*)-3,4,5-trihydroxy-6-(hydroxymethyl) tetrahydro-2*H*-pyran-2-yl)-9*H*-xanthen-9-one-3,6,7-triyl) pentanoyl L-proline methyl ester (G4). Yellow amorphous powder. Yield: 0.27 g (36.0%). ¹H NMR (600 MHz, DMSO-*d*₆), δ 13.57 (1H, s, OH), 7.46 (1H, s, H-8), 7.16 (1H, s, H-5), 6.61 (1H, s, H-4), 4.90 (1H, d, *J* = 5.5 Hz, H-1'), 4.62 (2H, d, *J* = 4.6 Hz, OH × 2), 4.45 (1H, t, *J* = 5.8 Hz, OH), 4.28 (3H, m, CH × 3), 4.16 (1H, s, CH), 4.10 (6H, m, OCH₂ × 3), 4.05 (1H, t, OH), 3.63–3.49 (20H, m, CH₃ × 3, CH₂ × 4, CH × 3), 2.32–2.30 (6H, m, CH₂ × 3), 2.24–1.99 (6H, m, CH₂ × 3), 1.92–1.89 (6H, m, CH₂ × 3), 1.83–1.79 (6H, m, CH₂ × 3), 1.60–1.56 (6H, m, CH₂ × 3), 1.50–1.45 (6H, m, CH₂ × 3). ¹³C NMR (151 MHz, DMSO), δ 179.2 (C-9), 172.7 (C=O × 3), 170.7 (C=O × 3), 165.0 (C-3), 160.4 (C-1), 156.8 (C-4a), 155.5 (C-6), 151.8 (C-4b), 146.1 (C-7), 112.2 (C-8a), 109.0 (C-8), 105.4 (C-2), 101.9 (C-5), 100.8 (C-9a), 91.0 (C-4), 81.8 (C-1'), 79.0 (C-5'), 72.5 (C-2'), 71.0 (C-3'), 70.4 (C-4'), 68.9 (–OCH₂–), 68.5 (–OCH₂–), 68.2 (–OCH₂–), 62.0 (C-6'), 51.7 (OCH₃ × 3), 46.5 (CH₂ × 3), 33.1 (CH₂), 33.0 (CH₂), 32.7 (CH₂), 28.8 (CH₂ × 3), 28.1 (CH₂), 28.0 (CH₂), 27.8 (CH₂), 24.4 (CH₂ × 3), 20.8 (CH₂), 20.8 (CH₂), 20.7 (CH₂). HRESIMS *m/z* 1078.4357 [M + Na]⁺ (calcd for C₅₂H₆₉N₃O₂₀Na, 1078.4367).

4.2.5 5-(1-Hydroxy-2-((3*R*,4*R*,5*S*,6*R*)-3,4,5-trihydroxy-6-(hydroxymethyl) tetrahydro-2*H*-pyran-2-yl)-9*H*-xanthen-9-one-3,6,7-triyl) pentanoyl L-leucine methyl ester (G5). Yellow amorphous powder. Yield: 0.28 g (35.4%). ¹H NMR (600 MHz, DMSO-*d*₆), δ 13.57 (1H, s, OH), 8.23 (3H, d, *J* = 7.8, 4.8 Hz, NH × 3), 7.47 (1H, s, H-8), 7.16 (1H, s, H-5), 6.61 (1H, s, H-4), 4.88 (1H, d, *J* = 4.4 Hz, H-1'), 4.62 (2H, m, OH × 2), 4.43 (1H, m, OH), 4.29 (3H, m, CH × 3), 4.26–3.95 (8H, m, CH₂ × 3, CH, OH), 3.71 (1H, m, CH–OH), 3.68–3.36 (13H, m, CH₃ × 3, CH₂, CH), 2.21 (6H, m, CH₂ × 3), 1.77 (6H, m, CH₂ × 3), 1.70 (6H, m, CH₂ × 3), 1.61–1.46 (9H, m, CH₂ × 3, CH × 3), 0.85 (18H, m, CH₃ × 6). ¹³C NMR (151 MHz, DMSO), δ 179.1 (C-9), 173.2 (C=O × 3), 172.3 (C=O × 3), 164.9 (C-3), 160.5 (C-1), 156.8 (C-4a), 155.5 (C-6), 151.8 (C-10a), 146.2 (C-7), 112.2 (C-8a), 109.0 (C-2), 105.5 (C-8), 102.5, 101.9 (C-5), 100.8 (C-9a), 91.0, 90.6 (C-4), 81.8 (C-1'), 79.3 (C-5'), 72.5 (C-2'), 71.1 (C-3'), 70.4 (C-4'), 68.7 (OCH₂), 68.5 (OCH₂), 68.0 (OCH₂), 62.0 (C-6'), 51.7 (CH–NH × 3), 50.2 (CH₃ × 3), 34.8 (CH₂–CO), 34.5 (CH₂–CO), 34.3 (CH₂–CO), 27.9 (CH₂), 27.9 (CH₂), 27.8 (CH₂), 24.3 (CH × 3), 22.8 (CH₃ × 9), 21.2 (CH₂ × 3). HRESIMS *m/z* 1126.5284 [M + Na]⁺ (calcd for C₅₅H₈₁N₃O₂₀Na, 1126.5306).

4.2.6 5-(1-Hydroxy-2-((3*R*,4*R*,5*S*,6*R*)-3,4,5-trihydroxy-6-(hydroxymethyl) tetrahydro-2*H*-pyran-2-yl)-9*H*-xanthen-9-one-3,6,7-triyl) pentanoyl L-isoleucine methyl ester (G6). Yellow amorphous powder. Yield: 0.35 g (44.3%). ¹H NMR (600 MHz, DMSO-*d*₆), δ 13.57 (1H, s, OH), 8.15 (3H, d, NH × 3), 7.47 (1H, s, H-8), 7.16 (1H, s, H-5), 6.61 (1H, s, H-4), 4.84 (1H, d, H-1'), 4.62 (2H, s, OH × 2), 4.42 (1H, d, *J* = 5.9 Hz, OH), 4.23 (3H, m, CH × 3), 4.21–3.99 (8H, m, CH₂ × 3, CH, OH), 3.70 (1H, m, H-3'), 3.62 (9H, s, CH₃ × 3), 3.13 (4H, m, H-4', H-5', H-6'), 2.25

(6H, m, CH₂ × 3), 1.77 (6H, m, CH₂ × 3), 1.68 (6H, m, CH₂ × 3), 1.30 (6H, m, CH₂ × 3), 0.83 (18H, q, *J* = 8.2, 7.5 Hz, CH₃ × 6). ¹³C NMR (150 MHz, DMSO), δ 179.2 (C-9), 172.4 (C=O × 3), 172.3 (C=O × 3), 164.9 (C-3), 160.5 (C-1), 156.9 (C-4a), 155.5 (C-6), 151.8 (C-10a), 146.2 (C-7), 112.2 (C-8a), 109.0 (C-2), 105.5 (C-8), 101.9 (C-5), 100.8 (C-9a), 91.0 (C-4), 81.8 (C-1'), 79.2 (C-5'), 72.5 (C-2'), 71.1 (C-3'), 70.4 (C-4'), 68.7 (–OCH₂–), 68.3 (–OCH₂–), 68.0 (–OCH₂–), 62.1 (C-6'), 56.3 (CO–CH × 3), 51.6 (OCH₃ × 3), 36.2 (CH–CH₃ × 3), 34.3 (CO–CH₂ × 3), 27.8 (CH₂ × 3), 24.9 (CH₂ × 3), 21.8 (CH₂ × 3), 15.5 (CH₃ × 3), 11.1 (CH₃ × 3). HRESIMS *m/z* 1126.5321 [M + Na]⁺ (calcd for C₅₅H₈₁N₃O₂₀Na, 1126.5306).

4.2.7 5-(1-Hydroxy-2-((3*R*,4*R*,5*S*,6*R*)-3,4,5-trihydroxy-6-(hydroxymethyl) tetrahydro-2*H*-pyran-2-yl)-9*H*-xanthen-9-one-3,6,7-triyl) pentanoyl L-valine methyl ester (G7). Yellow amorphous powder. Yield: 0.36 g (47.4%). ¹H NMR (600 MHz, DMSO-*d*₆), δ 13.56 (1H, d, *J* = 23.2 Hz, OH), 8.10 (3H, dd, *J* = 8.2, 3.4 Hz, NH × 3), 7.46 (1H, d, *J* = 2.2 Hz, H-8), 7.16 (1H, d, *J* = 2.0 Hz, H-5), 6.61 (1H, d, *J* = 12.5 Hz, H-4), 4.91 (2H, s, H-1'), 4.67–4.57 (2H, m, OH × 2), 4.46 (1H, dt, *J* = 19.3, 5.9 Hz, OH), 4.24–3.98 (11H, m, CH₂ × 3, CH, OH), 3.62 (11H, d, *J* = 5.3 Hz, CH₃ × 3, H-3'), 3.20–3.02 (3H, m, H-4', H-5', H-6'), 2.24–2.16 (6H, m, CO–CH₂ × 3), 2.03–1.98 (3H, m, NH–CH × 3), 1.81–1.73 (6H, m, CH₂ × 3), 1.62–1.55 (6H, m, CH₂ × 3), 1.47–1.38 (6H, m, CH₂ × 3), 0.89–0.84 (18H, m, CH₃ × 9). ¹³C NMR (150 MHz, DMSO), δ 179.1 (C-9), 172.6 (C=O × 3), 172.3 (C=O × 3), 165.0 (C-3), 160.4 (C-1), 156.8 (C-4a), 155.5 (C-6), 151.8 (C-4b), 146.0 (C-7), 112.2 (C-8a), 109.0 (C-8), 105.5 (C-2), 102.5 (C-9a), 101.9 (C-9a), 91.0 (C-4), 81.7 (C-1'), 79.3 (C-5'), 72.5 (C-2'), 71.0 (C-3'), 70.4 (C-4'), 69.0 (CH₂), 68.7 (CH₂), 68.3 (CH₂), 62.0 (C-6'), 57.4 (NH–CH × 3), 51.6 (OCH₃ × 3), 34.8 (CO–CH₂ × 3), 29.8 (NH–CH × 3), 19.0 (CH₃ × 3), 18.3 (CH₃ × 3). HRESIMS *m/z* 1084.4822 [M + Na]⁺ (calcd for C₅₂H₇₅N₃O₂₀Na, 1084.4836).

4.2.8 5-(1-Hydroxy-2-((3*R*,4*R*,5*S*,6*R*)-3,4,5-trihydroxy-6-(hydroxymethyl) tetrahydro-2*H*-pyran-2-yl)-9*H*-xanthen-9-one-3,6,7-triyl) pentanoyl L-tryptophan methyl ester (G8). Yellow amorphous powder. Yield: 0.25 g (26.6%). ¹H NMR (600 MHz, DMSO-*d*₆), δ 13.59 (1H, s, OH-1), 10.86 (3H, d, *J* = 5.0 Hz, NH), 8.30 (3H, d, NH). The benzene ring [7.50 (3H, d, *J* = 4.2 Hz), 7.34 (3H, d), 7.16 (4H, d, *J* = 2.9 Hz), 7.06 (3H, dd, *J* = 7.6, 2.8 Hz), 6.99 (3H, dd, *J* = 6.6, 2.7 Hz), 6.59 (1H, s)], 3.37–4.90 (OH, CH₂, OCH₂, OCH₃, CH), 1.66–2.19 (CH₂). ¹³C NMR (150 MHz, DMSO-*d*₆), δ 179.1 (C-9), 172.6 (C=O), 172.2 (C=O), 164.9 (C-3), 160.4 (C-1), 156.9 (C-4a), 155.4 (C-6), 151.8 (C-10a), 146.2 (C-7). The benzene ring [136.1, 127.1, 121.0, 118.4, 118.0, 111.5], 123.7 (C=CH), 112.2 (C-8a), 109.6 (C=CH), 109.0 (C-8), 105.5 (C-2), 102.0 (C-5), 100.7 (C-9a), 91.0 (C-4), 81.8 (C-1'), 79.0 (C-5'), 72.5 (C-2'), 71.0 (C-3'), 70.4 (C-4'), 68.7 (OCH₂), 68.3 (OCH₂), 67.9 (OCH₂), 62.0 (C-6'), 53.0 (NH–CH), 51.8 (OCH₃), 34.4 (CO–CH₂), 34.4 (CO–CH₂), 34.3 (CO–CH₂), 27.8 (CH₂), 27.6 (CH₂), 27.5 (CH₂), 27.1 (CH₂ × 3), 21.7 (CH₂), 21.6 (CH₂), 21.2 (CH₂). HRESIMS *m/z* 1345.5120 [M + Na]⁺ (calcd for C₇₀H₇₈O₂₀N₆Na, 1345.5163).

4.2.9 5-(1-Hydroxy-2-((3*R*,4*R*,5*S*,6*R*)-3,4,5-trihydroxy-6-(hydroxymethyl) tetrahydro-2*H*-pyran-2-yl)-9*H*-xanthen-9-one-

3,6,7-triyl) pentanoyl L-glycine methyl ester (G9). Yellow amorphous powder. Yield: 0.30 g (44.8%). ^1H NMR (600 MHz, $\text{DMSO}-d_6$), δ 13.56 (1H, d, $J = 19.8$ Hz, OH), 8.31 (3H, dd, $J = 5.8, 3.5$ Hz, $\text{NH} \times 3$), 7.47 (1H, d, $J = 1.9$ Hz, H-8), 7.16 (1H, s, H-5), 6.61 (1H, d, $J = 12.5$ Hz, H-4), 4.10 (5H, dt, $J = 18.7, 6.3$ Hz, H-1', $\text{OH} \times 3$), 3.87–3.65 (14H, m, $\text{CH}_2 \times 3$, $\text{CH}_2 \times 3$, OH, H-2'), 3.62 (14H, m, $\text{OCH}_3 \times 3$, H-3', H-4', H-5', H-6'), 2.25–2.22 (6H, m, $\text{CH}_2 \times 3$), 1.81–1.77 (6H, m, $\text{CH}_2 \times 3$), 1.71–1.67 (6H, m, $\text{CH}_2 \times 3$). ^{13}C NMR (150 MHz, DMSO), δ 179.3 (C-9), 172.7 ($\text{C}=\text{O} \times 3$), 170.6 ($\text{C}=\text{O} \times 3$), 165.0 (C-3), 164.0 (C-1), 156.9 (C-4a), 155.5 (C-6), 151.8 (C-4b), 146.2 (C-7), 112.3 (C-8a), 109.0 (C-8), 105.5 (C-2), 102.5 (C-5), 100.8 (C-9a), 90.6 (C-4), 81.8 (C-1'), 79.2 (C-5'), 72.6 (C-2'), 71.0 (C-3'), 70.5 (C-4'), 68.8 (CH_2), 68.5 (CH_2), 68.4 (CH_2), 62.0 (C-6'), 51.7 ($\text{OCH}_3 \times 3$), 40.6 ($\text{NH}-\text{CH}_2$), 34.5 ($\text{CH}_2 \times 3$), 27.8 ($\text{CH}_2 \times 3$), 21.8 ($\text{CH}_2 \times 3$). HRESIMS m/z 958.3425 $[\text{M} + \text{Na}]^+$ (calcd for $\text{C}_{43}\text{H}_{57}\text{O}_{20}\text{N}_3\text{Na}$, 958.3428).

4.2.10 6-(1-Hydroxy-2-((3R,4R,5S,6R)-3,4,5-trihydroxy-6-(hydroxymethyl) tetrahydro-2H-pyran-2-yl)-9H-xanthen-9-one-3,6,7-triyl) hexanoyl L-phenylalanine methyl ester (G10). Yellow amorphous powder. Yield: 0.25 g (28.1%). ^1H NMR (600 MHz, $\text{DMSO}-d_6$), δ 13.58 (1H, s, OH), 8.29 (3H, d, $J = 7.9$, 2.1 Hz, $\text{NH} \times 3$), 7.47 (1H, s, H-8), 7.28–7.18 (15H, m, $\text{CH} \times 15$), 7.15 (1H, s, H-5), 4.92 (1H, d, H-1'), 4.63 (2H, d, $\text{OH} \times 2$), 4.49 (3H, d, $\text{CH} \times 3$), 4.44 (1H, s, OH), 4.19–3.87 (8H, m, $\text{CH}_2 \times 3$, CH , OH), 3.78–3.39 (12H, m, $\text{CH}_3 \times 3$, $\text{CH} \times 3$), 3.19 (2H, m, CH_2), [3.03 (m, 3H), 2.87 (m, 3H), $\text{CH}_2 \times 3$], 2.09 (6H, m, $\text{CH}_2 \times 3$), 1.70 (6H, m, $\text{CH}_2 \times 3$), 1.48 (6H, m, $\text{CH}_2 \times 3$), 1.31 (6H, m, $\text{CH}_2 \times 3$). ^{13}C NMR (150 MHz, DMSO), δ 179.1 (C-9), 172.3 ($\text{C}=\text{O}$), 165.0 (C-3), 160.4 (C-1), 156.9 (C-4a), 155.5 (C-6), 151.8 (C-4b), 146.2 (C-7), 137.3 (C-1''), 129.1 (C-3'' $\times 3$, C-5'' $\times 3$), 128.2 (C-2'' $\times 3$, C-6'' $\times 3$), 126.5 (C-4'' $\times 3$), 112.2 (C-8a), 109.0 (C-8), 105.4 (C-2), 102.5 (C-5), 101.9 (C-9a), 91.0 (C-4), 82.0 (C-1'), 79.3, 79.0 (C-5'), 73.1 (C-2'), 71.0 (C-3'), 69.0 (CH_2), 68.6 (CH_2), 68.2 (CH_2), 62.1 (C-6'), 53.5 (NCH), 53.4 (NCH), 53.4 (NCH), 51.8 ($-\text{O}-\text{CH}_3 \times 3$), 36.7 ($\text{CH}_2 \times 3$), 34.9 (CH_2), 34.9 (CH_2), 34.9 (CH_2), 28.2 (CH_2), 28.2 (CH_2), 28.0 (CH_2), 28.0, (CH_2) 25.1 ($\text{CH}_2 \times 3$), 24.9 (CH_2), 24.9 (CH_2), 24.8, (CH_2). HRESIMS m/z 1270.5306 $[\text{M} + \text{Na}]^+$ (calcd for $\text{C}_{67}\text{H}_{81}\text{O}_{20}\text{N}_3\text{Na}$, 1270.5306).

4.2.11 6-(1-Hydroxy-2-((3R,4R,5S,6R)-3,4,5-trihydroxy-6-(hydroxymethyl) tetrahydro-2H-pyran-2-yl)-9H-xanthen-9-one-3,6,7-triyl) hexanoyl L-methionine methyl ester (G11). Yellow amorphous powder. Yield: 0.29 g (34.1%). ^1H NMR (600 MHz, $\text{DMSO}-d_6$), δ 13.57 (1H, s), 8.24 (6H, d, $J = 7.3$ Hz, NH), 7.49 (1H, s), 7.17 (1H, s), 6.61 (1H, s), 3.34–4.86 (OH, NCH, OCH_3 and OCH_2), 1.69–2.50 (SCH_3 , SCH_2 and CH_2). ^{13}C NMR (150 MHz, $\text{DMSO}-d_6$), δ 179.1 (C-9), 172.6 ($\text{C}=\text{O} \times 6$), 165.0 (C-3), 160.4 (C-1), 156.9 (C-4a), 154.2 (C-6), 150.3 (C-10a), 146.2 (C-7), 112.2 (C-8a), 109.0 (C-8), 100.8 (C-9a), 91.0 (C-4), 81.9 (C-1'), 79.2 (C-5'), 72.5 (C-2'), 71.0 (C-3'), 70.4 (C-4'), 69.0 (OCH_2), 68.8 (OCH_2), 68.7 (OCH_2), 62.0 (C-6'), 51.9 (NCH $\times 3$), 50.9 ($\text{OCH}_3 \times 3$), 35.0 ($\text{CO}-\text{CH}_2$), 34.9 ($\text{CO}-\text{CH}_2$), 34.9 ($\text{CO}-\text{CH}_2$), 30.5 ($\text{CH}_2 \times 3$), 29.6 ($\text{CH}_2 \times 3$), 28.4 ($\text{CH}_2 \times 3$), 25.3 (CH_2), 25.2 (CH_2), 25.1 (CH_2), 14.6 (CH_3), 14.6 (CH_3), 14.4 (CH_3). HRESIMS

m/z 1200.4666 $[\text{M} + \text{H}]^+$ (calcd for $\text{C}_{55}\text{H}_{82}\text{N}_3\text{O}_{20}\text{S}_3$, 1200.4648).

4.2.12 6-(1-Hydroxy-2-((3R,4R,5S,6R)-3,4,5-trihydroxy-6-(hydroxymethyl) tetrahydro-2H-pyran-2-yl)-9H-xanthen-9-one-3,6,7-triyl) hexanoyl L-alanine methyl ester (G12). Yellow amorphous powder. Yield: 0.34 g (46.6%). ^1H NMR (600 MHz, $\text{DMSO}-d_6$), δ 13.56 (1H, s, OH-1), 8.23 (3H, d, $J = 7.2$ Hz, $\text{NH} \times 3$), 7.47 (1H, s, H-8), 7.16 (1H, s, H-5), 6.61 (1H, s, H-4), 3.61 (9H, s, $\text{OCH}_3 \times 3$), 2.14 (6H, t, $J = 6.7$ Hz, $\text{CH}_2 \times 3$), 1.77 (6H, m, $\text{CH}_2 \times 3$), 1.58 (6H, m, $\text{CH}_2 \times 3$), 1.44 (6H, m, $\text{CH}_2 \times 3$), 1.25 (9H, m, $\text{CH}_3 \times 3$). ^{13}C NMR (150 MHz, $\text{DMSO}-d_6$), δ 179.1 (C-9), 173.4 ($\text{C}=\text{O} \times 3$), 172.1 ($\text{C}=\text{O} \times 3$), 165.0 (C-3), 160.4 (C-1), 156.8 (C-4a), 155.5 (C-6), 151.8 (C-10a), 146.2 (C-7), 112.2 (C-8a), 109.0 (C-8), 105.5 (C-2), 101.9 (C-5), 100.8 (C-9a), 91.0 (C-4), 81.7 (C-1'), 79.3 (C-5'), 72.5 (C-2'), 71.0 (C-3'), 70.4 (C-4'), 69.0 (OCH_2), 68.7 (OCH_2), 68.3 (OCH_2), 62.0 (C-6'), 51.8 ($\text{OCH}_3 \times 3$), 47.5 ($\text{NH}-\text{CH} \times 3$), 35.0 ($\text{CO}-\text{CH}_2$), 34.9 ($\text{CO}-\text{CH}_2$), 34.8 ($\text{CO}-\text{CH}_2$), 28.3 (CH_2), 28.3 (CH_2), 28.1 (CH_2), 25.3 (CH_2), 25.3 (CH_2), 25.2 (CH_2), 24.9 (CH_2), 24.8 (CH_2), 17.0 ($\text{CH}_3 \times 3$). HRESIMS m/z 1020.4548 $[\text{M} + \text{H}]^+$ (calcd for $\text{C}_{49}\text{H}_{70}\text{N}_3\text{O}_{20}$, 1020.4547).

4.2.13 6-(1-Hydroxy-2-((3R,4R,5S,6R)-3,4,5-trihydroxy-6-(hydroxymethyl) tetrahydro-2H-pyran-2-yl)-9H-xanthen-9-one-3,6,7-triyl) hexanoyl L-proline methyl ester (G13). Yellow amorphous powder. Yield: 0.29 g (37.2%). ^1H NMR (600 MHz, $\text{DMSO}-d_6$), δ 13.56 (1H, s, OH), 7.47 (1H, s, H-8), 7.16 (1H, s, H-5), 6.62 (1H, s, H-4), 4.86 (1H, t, $J = 4.3$ Hz, H-1'), 4.63 (2H, d, $J = 11.2$ Hz, $\text{OH} \times 2$), 4.42 (1H, m, OH), 4.29 (3H, m, $\text{CH} \times 3$), 4.23–3.99 (8H, m, $\text{CH}_2 \times 3$, CH , OH), 3.78–3.34 (20H, m, $\text{CH}_3 \times 3$, $\text{CH}_2 \times 4$, $\text{CH} \times 3$), 2.42–2.31 (6H, m, $\text{CH}_2 \times 3$), 2.14–1.75 (18H, m, $\text{CH}_2 \times 9$), 1.68 (6H, m, $\text{CH}_2 \times 3$). ^{13}C NMR (151 MHz, DMSO), δ 179.1 (C-9), 172.7 ($\text{C}=\text{O} \times 3$), 170.8 ($\text{C}=\text{O} \times 3$), 165.0 (C-3), 160.4 (C-1), 156.8 (C-4a), 155.6 (C-6), 151.8 (C-10a), 146.2 (C-7), 118.1 (C-8a), 112.2 (C-8a), 109.0 (C-2), 105.5 (C-8), 102.5, 101.9 (C-5), 100.8 (C-9a), 90.9 (C-4), 82.0 (C-1'), 79.3 (C-5'), 78.9, 72.5 (C-2'), 71.0 (C-3'), 70.4 (C-4'), 69.0 ($-\text{OCH}_2-$), 68.2 ($-\text{OCH}_2-$), 62.0 ($-\text{OCH}_2-$), 61.98 (C-6'), 51.7 ($\text{OCH}_3 \times 3$), 48.6 ($\text{CH}_2 \times 3$), 33.5 (CH_2), 33.4 (CH_2), 33.2 (CH_2), 28.8 ($\text{CH}_2 \times 3$), 28.5 (CH_2), 28.4 (CH_2), 28.1 (CH_2), 24.5 ($\text{CH}_2 \times 3$), 23.9 (CH_2), 23.9 (CH_2), 23.8 (CH_2). HRESIMS m/z 1120.4839 $[\text{M} + \text{Na}]^+$ (calcd for $\text{C}_{55}\text{H}_{75}\text{N}_3\text{O}_{20}\text{Na}$, 1120.4836).

4.2.14 6-(1-Hydroxy-2-((3R,4R,5S,6R)-3,4,5-trihydroxy-6-(hydroxymethyl) tetrahydro-2H-pyran-2-yl)-9H-xanthen-9-one-3,6,7-triyl) hexanoyl L-leucine methyl ester (G14). Yellow amorphous powder. Yield: 0.30 g (37.0%). ^1H NMR (600 MHz, $\text{DMSO}-d_6$), δ 13.56 (1H, s, OH), 8.18 (3H, d, $J = 7.8$ Hz, $\text{NH} \times 3$), 7.46 (1H, s, H-8), 7.16 (1H, s, H-5), 6.61 (1H, s, H-4), 4.90 (1H, d, $J = 5.4$ Hz, H-1'), 4.62 (2H, m, $\text{OH} \times 2$), 4.44 (1H, m, OH), 4.27 (3H, m, $\text{CH} \times 3$), 4.19–3.96 (8H, m, $\text{CH}_2 \times 3$, CH , OH), 3.74 (1H, dd, $J = 10.9, 5.9$ Hz, CH), 3.61 (13H, d, $J = 5.2$ Hz, $\text{CH}_3 \times 3$, CH_2 , CH), 2.15 (6H, m, $\text{CH}_2 \times 3$), 1.78 (6H, m, $\text{CH}_2 \times 3$), 1.59 (6H, m, $\text{CH}_2 \times 3$), 1.54 (6H, m, $\text{CH}_2 \times 3$), 1.47 (3H, m, $\text{CH} \times 3$), 1.44 (6H, m, $\text{CH}_2 \times 3$), 0.85 (18H, m, $\text{CH}_3 \times 6$). ^{13}C NMR (151 MHz, DMSO), δ 179.1 (C-9), 173.3 ($\text{NH}-\text{CO}$), 173.2 ($\text{NH}-\text{CO}$), 173.2 ($\text{NH}-\text{CO}$), 172.4 ($\text{CO}-\text{CH}_3$), 172.4 ($\text{CO}-\text{CH}_3$), 172.4 ($\text{CO}-\text{CH}_3$), 165.0 (C-3), 161.4 (C-1),

156.8 (C-4a), 155.5 (C-6), 151.8 (C-10a), 146.2 (C-7), 112.2 (C-8a), 109.0 (C-2), 105.5 (C-8), 101.9 (C-5), 100.8 (C-9a), 90.9 (C-4), 81.7 (C-1'), 79.0 (C-5'), 72.5 (C-2'), 71.0 (C-3'), 70.4 (C-4'), 68.7 (–OCH₂– × 3), 62.0 (C-6'), 51.7 (CH–NH × 3), 50.1 (CH₃ × 3), 34.9 (CH₂–CO), 34.9 (CH₂–CO), 34.9 (CH₂–CO), 28.3 (CH₂), 28.3 (CH₂), 28.2 (CH₂), 25.0 (CH₂), 25.0 (CH₂), 24.9 (CH₂), 24.3 (CH₂ × 3), 22.7 (CH₂ × 3), 21.2 (CH₃ × 9). HRESIMS *m/z* 1168.5748 [M + Na]⁺ (calcd for C₅₈H₈₇N₃O₂₀Na, 1168.5775).

4.2.15 6-(1-Hydroxy-2-((3*R*,4*R*,5*S*,6*R*)-3,4,5-trihydroxy-6-(hydroxymethyl) tetrahydro-2*H*-pyran-2-yl)-9*H*-xanthen-9-one-3,6,7-triyl) hexanoyl L-isoleucine methyl ester (G15). Yellow amorphous powder. Yield: 0.26 g (32.1%). ¹H NMR (600 MHz, DMSO-*d*₆), δ 13.56 (1H, s, OH), 8.11 (3H, d, *J* = 7.9 Hz, NH × 3), 7.46 (1H, s, H-8), 7.16 (1H, s, H-5), 6.61 (1H, s, H-4), 4.94 (1H, s, H-1'), 4.63 (2H, s, OH × 2), 4.46 (1H, d, *J* = 19.6 Hz, OH), 4.22 (3H, dd, *J* = 7.3 Hz, NH–CH), 4.17–4.00 (8H, m, CH₂, CH, OH), 3.71 (1H, s, H-3'), 3.41–2.99 (13H, m, CH₃ × 3, H-4', H-5', H-6'), 2.23–2.16 (6H, m, CH₂ × 3), 1.78–1.74 (6H, m, CH₂ × 3), 1.60–1.55 (6H, m, CH₂ × 3), 1.44–1.16 (12H, m, CH₂ × 6), 0.85–0.83 (9H, m, CH₃ × 3), 0.82–0.78 (9H, m, CH₃ × 3). ¹³C NMR (150 MHz, DMSO), δ 179.1 (C-9), 172.5 (C=O × 3), 172.3 (C=O × 3), 165.0 (C-3), 160.4 (C-1), 156.8 (C-4a), 155.5 (C-6), 151.8 (C-10a), 146.2 (C-7), 112.2 (C-8a), 109.0 (C-2), 105.5 (C-8), 101.9 (C-5), 100.7 (C-9a), 91.0 (C-4), 81.8 (C-1'), 79.1 (C-5'), 72.5 (C-2'), 71.0 (C-3'), 70.4 (C-4'), 69.0 (–OCH₂–), 68.7 (–OCH₂–), 68.3 (–OCH₂–), 62.0 (C-6'), 56.2 (CO–CH × 3), 51.5 (OCH₃ × 3), 39.9, 39.8, 39.7, 39.5, 39.4, 39.2, 39.1, 36.2 (CH–CH₃ × 3), 34.8 (CO–CH₂ × 3), 28.3 (CH₂), 28.2 (CH₂), 28.0 (CH₂), 25.2 (CH₂), 25.1 (CH₂), 25.0 (CH₂), 25.0 (CH₂), 25.0 (CH₂), 24.9 (CH₂), 24.8 (CH₂ × 3), 15.5 (CH₃ × 3), 11.0 (CH₃ × 3). HRESIMS *m/z* 1168.5785 [M + Na]⁺ (calcd for C₅₈H₈₇N₃O₂₀Na, 1168.5775).

4.2.16 6-(1-Hydroxy-2-((3*R*,4*R*,5*S*,6*R*)-3,4,5-trihydroxy-6-(hydroxymethyl) tetrahydro-2*H*-pyran-2-yl)-9*H*-xanthen-9-one-3,6,7-triyl) hexanoyl L-valine methyl ester (G16). Yellow amorphous powder. Yield: 0.26 g (32.9%). ¹H NMR (600 MHz, DMSO-*d*₆), δ 13.56 (1H, s, OH), 8.10 (3H, d, *J* = 8.0 Hz, NH × 3), 7.46 (1H, s, H-8), 7.16 (1H, s, H-5), 6.61 (1H, s, H-4), 4.92 (1H, s, H-1'), 4.62 (2H, s, OH × 2), 4.45 (1H, d, OH), 4.17 (3H, m, CH × 3), 4.16–3.99 (8H, m, CH₂ × 3, CH, OH), 3.72 (1H, m, H-3'), 3.62 (9H, s, CH₃ × 3), 3.22–3.00 (4H, m, H-4', H-5', H-6'), 2.20 (6H, m, CO–CH₂ × 3), 2.01 (3H, m, NH–CH × 3), 1.77 (6H, m, CH₂ × 3), 1.58 (6H, m, CH₂ × 3), 1.43 (6H, m, CH₂ × 3), 0.87 (18H, m, CH₃ × 9). ¹³C NMR (150 MHz, DMSO), δ 179.1 (C-9), 172.6 (C=O × 3), 172.3 (C=O × 3), 165.0 (C-3), 160.4 (C-1), 156.9 (C-4a), 155.5 (C-6), 151.8 (C-4b), 146.2 (C-7), 112.2 (C-8a), 109.0 (C-8), 105.5 (C-2), 101.9 (C-9a), 81.7 (C-1'), 79.3 (C-5'), 72.5 (C-2'), 71.0 (C-3'), 70.4 (C-4'), 69.0 (CH₂), 68.7 (CH₂), 68.3 (CH₂), 62.0 (C-6'), 57.4 (NH–CH × 3), 51.6 (OCH₃ × 3), 34.8 (CO–CH₂ × 3), 29.8 (NH–CH × 3), 28.1 (CH₂ × 3), 25.3 (CH₂), 25.1 (CH₂), 25.1 (CH₂), 25.0 (CH₂), 25.0 (CH₂), 25.0 (CH₂), 19.0 (CH₃ × 3), 18.3 (CH₃ × 3). HRESIMS *m/z* 1126.5302 [M + Na]⁺ (calcd for C₅₅H₈₁N₃O₂₀Na, 1126.5306).

4.2.17 6-(1-Hydroxy-2-((3*R*,4*R*,5*S*,6*R*)-3,4,5-trihydroxy-6-(hydroxymethyl) tetrahydro-2*H*-pyran-2-yl)-9*H*-xanthen-9-one-3,6,7-triyl) hexanoyl L-tryptophan methyl ester (G17). Yellow amorphous powder. Yield: 0.27 g (27.8%). ¹H NMR (600 MHz, DMSO-*d*₆), δ 13.60 (1H, s, OH-1), 10.86 (3H, s, NH), 8.26 (3H, d, *J* = 4.4 Hz, NH). The benzene ring [7.50 (3H, d), 7.34 (3H, d, *J* = 4.5 Hz), 7.15 (4H, d, *J* = 8.5 Hz), 7.05 (3H, q, *J* = 8.5 Hz), 6.98 (3H, q), 6.60 (1H, s)], 4.66 (1H, d, *J* = 10.0 Hz, H-1'), 3.08–4.53 (OH, OCH₃, OCH₂, CH₂), 2.13 (6H, t, CO–CH₂), 1.72 (6H, m, CH₂), 1.51 (6H, m, CH₂), 1.34 (6H, m, CH₂). ¹³C NMR (150 MHz, DMSO-*d*₆), δ 179.4 (C-9), 172.6 (NH–CO), 172.3 (CH–CO), 165.0 (C-3), 160.4 (C-1), 156.9 (C-4a), 155.5 (C-6), 151.8 (C-4a), 146.2 (C-7). The benzene ring [136.1, 127.1, 121.0, 118.4, 118.0, 111.4], 123.7 (C=CH × 3), 112.2 (C-8a), 109.6 (C=CH), 109.0 (C-8), 105.5 (C-2), 102.0 (C-5), 100.7 (C-9a), 91.0 (C-4), 81.7 (C-1'), 79.0 (C-5'), 72.5 (C-2'), 71.0 (C-3'), 70.4 (C-4'), 69.0 (OCH₂), 68.6 (OCH₂), 68.3 (OCH₂), 62.0 (C-6'), 53.0 (NH–CH × 3), 51.8 (OCH₃ × 3), 35.0 (CO–CH₂), 34.9 (CO–CH₂), 34.9 (CO–CH₂), 28.3 (CH₂ × 3), 28.0 (CH₂ × 3), 25.2 (CH₂), 25.0 (CH₂), 25.0 (CH₂), 24.9 (CH₂), 24.8 (CH₂), 24.8 (CH₂). HRESIMS *m/z* 1387.5593 [M + Na]⁺ (calcd for C₇₃H₈₄O₂₀N₆Na, 1387.5633).

4.2.18 6-(1-Hydroxy-2-((3*R*,4*R*,5*S*,6*R*)-3,4,5-trihydroxy-6-(hydroxymethyl) tetrahydro-2*H*-pyran-2-yl)-9*H*-xanthen-9-one-3,6,7-triyl) hexanoyl L-glycine methyl ester (G18). Yellow amorphous powder. Yield: 0.24 g (34.3%). ¹H NMR (600 MHz, DMSO-*d*₆), δ 13.57 (1H, s, OH), 8.29 (3H, t, NH × 3), 7.47 (1H, s, H-8), 7.17 (1H, s, H-5), 6.62 (1H, s, H-4), 4.93 (1H, d, *J* = 5.3 Hz, H-1'), 4.64 (2H, s, OH × 2), 4.48 (1H, d, *J* = 21.6, 5.9 Hz, OH), 4.13 (6H, m, CH₂ × 3), 3.82 (6H, d, *J* = 5.8 Hz, CH₂ × 3), 3.73 (1H, m, OH), 3.69–3.49 (14H, m, OCH₃, H-4', H-5', H-6'), 2.18 (6H, m, CH₂ × 3), 1.78 (6H, m, CH₂ × 3), 1.59 (6H, m, CH₂ × 3), 1.45 (6H, m, CH₂ × 3). ¹³C NMR (151 MHz, DMSO), δ 179.1 (C-9), 172.7 (C=O × 3), 170.5 (C=O × 3), 165.0 (C-3), 160.4 (C-1), 156.9 (C-4a), 155.5 (C-6), 151.9 (C-4b), 146.2 (C-7), 112.2 (C-8a), 109.0 (C-8), 105.5 (C-2), 102.5 (C-5), 101.9 (C-9a), 90.6 (C-4), 81.7 (C-1'), 79.0 (C-5'), 72.5 (C-2'), 70.9 (C-3'), 70.4 (C-4'), 69.0 (CH₂), 68.7 (CH₂), 68.3 (CH₂), 60.6 (C-6'), 51.6 (OCH₃ × 3), 40.5 (NH–CH₂), 34.9 (CH₂ × 3), 31.2 (CH₂ × 3), 29.8 (CH₂ × 3), 24.9 (CH₂ × 3). HRESIMS *m/z* 1000.3891 [M + Na]⁺ (calcd for C₄₆H₆₃O₂₀N₃Na, 1000.3897).

4.3 Cell proliferation assay

The 3T3-L1 preadipocytes were from American Tissue Culture Collection (ATCC, Manassas, VA, USA). They were cultured in DMEM medium (GIBCO, NY, USA), containing 10% (v/v) fetal bovine serum (GIBCO, NY, USA) and 1% penicillin–streptomycin–amphotericin B solution at 37 °C with 5% CO₂. To induce differentiation, the 3T3-L1 cells were cultured in the growth medium³⁷ until the bottom of the flasks was covered. They were then cultured for a further two days to allow the cells to exit the cell cycle through contact inhibition. The culture medium was then changed to differentiation medium (the growth medium with methyl isobutylxanthine (0.5 mM), dexamethasone (1 μM) and

insulin ($10 \mu\text{g mL}^{-1}$), and after 48 hours, the medium was changed again to maintenance medium.³⁸ The cells were cultured in normal DMEM for four days, with the medium changed every two days.

The viability of the cells was evaluated using MTT assay.³⁹ The 3T3-L1 preadipocytes were inoculated into 96-well plates at a 8000 cells per well density for 24 h. Following a 24 h incubation period, the cells were treated with varying concentrations of the drugs ($0\text{--}500 \mu\text{M}$) for a further 48 h. Subsequently, $20 \mu\text{L}$ MTT (5 mg mL^{-1}) was added and incubated for 4 h. Following this, the MTT was removed. The wells were supplemented with $150 \mu\text{L}$ dimethyl sulfoxide (DMSO) and agitated for 10 min to facilitate complete dissolution of the formazan crystals. The absorbance at 490 nm was then determined using a microplate reader (ELx800, BioTek, USA).

4.4 Solubility experiments

The equilibrium solubility curve was tested by the shake flask method. A solution of $100 \mu\text{g mL}^{-1}$ MGF was prepared as a control and diluted with water saturated with *n*-octanol to obtain solutions of 50, 25, 12.5, 6.25, 3.125, and $1.5625 \mu\text{g mL}^{-1}$ of MGF control solution. An accurate 1 mg mL^{-1} solution of the derivative control was prepared by dilution with saturated octanol, resulting in a solution of 100, 50, 25, 12.5, 6.25, and $3.125 \mu\text{g mL}^{-1}$ of the derivative control solution. The standard curve was scanned using a UV spectrophotometer within the wavelength range of 200–500 nm. Subsequently, linear regression was performed by plotting the standard curve with the mass concentration of the compounds as the horizontal coordinate and the absorbance at the maximum absorption wavelength as the vertical coordinate.

The lipophilicity of the acylated derivatives was evaluated by determining the octanol/water partition coefficient ($\log P$). In summary, water and *n*-octanol were saturated with each other (1:1, v/v) for 24 hours. The samples were then dissolved in water-saturated *n*-octanol, and the absorbance at 264 nm was measured by a UV spectrophotometer (SPECIRD S-600, Analytic Jena, Germany). Subsequently, *n*-octanol-saturated water was added, and the mixture was shaken vigorously for one hour and then centrifuged at 2000 rpm for ten minutes. The absorbance of the upper layer of *n*-octanol was determined at 264 nm. The octanol/water partition coefficients were calculated using the equation: $\log P = \log C_X / (C_0 - C_X)$.

4.5 FASN activity assay

Cells in the logarithmic growth phase were inoculated into 6-well plates at a cell density of 1×10^4 cells per mL. The culture was continued until the cells reached 70–80% confluence in DMEM complete medium. Thereafter, different concentrations of the drug-containing medium were added in the form of liquid exchange. Three replicate wells were set up in each group, and the culture was continued for 48 h.

The cells in the plate were resuspended and counted to the same density, and the extract was then added. Following the resuspension and counting of the cells to the same density, the appropriate volume of extraction solution was added (1 mL of extraction solution for 5 million cells). The cells were then broken by ultrasonication in an ice bath (power of 300 W, ultrasonication for 3 s, interval of 7 s, total time of 3 min), and subsequently centrifuged at $12000g$ in 4°C for 40 min. Subsequently, the extract was quantified by the FASN activity assay kit.

4.6 Molecular docking

As the structure of mouse FASN (UniProt ID: P19096) has not been determined, we predict the mouse FASN structure using AlphaFold3 and superpose it with some FASN crystal structures reported in the RCSB to identify the ligand binding site and set the stage for subsequent binding pocket selection. We preprocess the protein with MGLTools software (version 1.5.7),⁴⁰ including adding hydrogen atoms, and convert the protein and small molecules into PDBQT format. Referring to the ligand in the crystal structure, we set the binding pocket center coordinates and grid size. Molecular docking simulations are performed using AutoDock Vina software (version 1.1.2)⁴¹ with default parameters. Based on binding free energy, we screen the conformations with the strongest affinity for subsequent molecular dynamics simulations.

4.7 Molecular dynamics simulations

The MD simulations of the protein–ligand complex were performed using GROMACS 2024.3 software. Before simulation, the protein structure is truncated to an appropriate size. For the protein, we use the Amber14SB force field, the TIP3P model for water molecules, and generate ligand topological parameters *via* the Antechamber Python Parser Interface (ACPYPE) tool based on the GAFF force field. The ligand–protein complex system is placed in a periodic boundary octahedral box with TIP3P water molecules. Na^+ and Cl^- ions are added to adjust the system to a physiological salt concentration of 0.150 mol L^{-1} and neutralize the total charge. After system construction, we first perform 50 000 steps of steepest descent energy minimization to eliminate unrealistic conformations. Then, we conduct two system equilibration stages: 100 ps of NVT (constant number of particles, volume, and temperature) and 100 ps of NPT (constant number of particles, pressure, and temperature) simulations. During this time, positional restraints are applied to the protein backbone heavy atoms to maintain protein stability. The temperature is kept at 300 K using the V-rescale thermostat algorithm, and the pressure is controlled at 1 bar *via* the Parrinello–Rahman algorithm. After equilibration, we carry out a 100 ns production simulation. All positional restraints are removed during this phase. With a 2 fs time step for trajectory integration and the particle mesh Ewald (PME) method for long-range

electrostatic interactions,⁴² we save trajectories every 10 ps, resulting in 10 000 frames for subsequent analysis. Stability trajectories during the late stage (90–100 ns) of the simulation were extracted, and binding free energy calculations were performed on the ligand–protein complexes using the gmx_MMPBSA tool (version 1.4.3).

4.8 Oil red O staining in 3T3-L1 cells

At the conclusion of the induced differentiation process, the previous medium was removed, the cells were rinsed with PBS, and 10% paraformaldehyde was added over 20 minutes to facilitate fixation. Following this, the paraformaldehyde fixative was discarded and the cells were rinsed with PBS. Subsequently, the cells were washed with staining wash solution, stained with staining solution for 20 minutes, and then washed with staining wash solution. Finally, they were added to PBS for observation under a microscope. Subsequently, PBS was removed and isopropanol was added to facilitate dissolution of the fat droplets and the oil red O staining solution for a period of 10 minutes. Thereafter, the absorbance at 510 nm was determined.⁴³

4.9 ROS assay

The DCFH-DA solution was diluted with serum-free culture medium to a final concentration of 10 μM . The cell culture medium was then removed, and the diluted DCFH-DA solution was added. The cells were incubated for 20 min at 37 °C. The cells were washed to ensure the complete removal of DCFH-DA that had not entered the cells. The fluorescence intensity of the cells was then tested by flow cytometry and photographed with a fluorescence inverted microscope (Leica DMI8, USA).

4.10 Cell cycle assay

Contact-inhibited 3T3-L1 preadipocytes were induced to differentiate using MDI (3-isobutyl-1-methylxanthine, dexamethasone and insulin) in the presence of compounds **G1**, MGF and orlistat for 24 h. Then, the cells were fixed with 70% ethanol overnight, before being centrifuged to remove ethanol and washed with PBS. A volume of 0.5 mL of propidium iodide staining solution was added to each tube of cell samples, and the cellular precipitates were resuspended slowly and fully. The cells were then warmed in the temperature bath at 37 °C, away from light, for 30 min. Subsequently, flow cytometry was conducted.

4.11 Plasma stability assay

Pipette 2 μL of the test drug, add it to 198 μL of plasma, and mix well. Then, incubate at 37 °C in a water bath. Take samples at 0, 1, 3, 6, and 12 h. After each sampling, add an equal volume of ice-cold acetonitrile to precipitate the protein. Centrifuge at 12 000 rpm for 5 min, and collect the supernatant for detection.

4.12 Liver microsomal stability assay

The incubation system was set up as described in the literature.⁴⁴ To 188 μL of PBS buffer in an ice bath, 12 μL of NADPH (10 μL of solution A and 2 μL of solution B) was added, followed by 2 μL of compound **G1**. After incubation for 5 min at 37 °C in a water bath, 5 μL of hepatic microsomal enzyme from SD rats was added, and the mixture was incubated at 37 °C in a water bath. At the time points of 0.5, 15, 30, 45, 60, and 90 min, 400 μL of ice-cold acetonitrile was added to terminate the reaction.

4.13 Animals and experimental design

Six-week-old male C57BL/6J mice were obtained from Jinan Pengyue Experimental Animal Breeding Co., Ltd. (Jinan, China) with license number SCXK (Lu) 2019-0003. Mice were randomly divided into 5 groups of 6 mice each and raised in plastic cages, allowing food and water freely under control conditions (20–25 °C, 40–70% humidity, and 12 h light/12 h dark cycles). After adaptive feeding (normal diet, AIN-93M diet containing 11.8% fat energy supply ratio, from Cooperative Medical Biological Engineering Co., Ltd., Jiangsu, China) for seven days, mice were administered with different diet. One group was provided with normal diet (NC). The remaining four groups were fed with high-fat diet (HFD, 45.0% fat energy supply ratio, from Cooperative Medical Biological Engineering Co., Ltd., Jiangsu, China) and high-sugar drinking water (20.0% sugar). The body weight was monitored on a weekly basis. The success of the modelling was determined when the body weight of the HFD group was found to be greater than that of the NC group by a factor of 15%. Compound **G1** and orlistat were suspended in 1% CMC-Na. The orlistat group were given intraperitoneally 30 mg kg⁻¹/2 days orlistat, G1-I and G1-II groups were given intraperitoneally 30 and 60 mg kg⁻¹/2 days compound **G1** respectively, and the HFD group was given intraperitoneally the same volume of 1% CMC-Na. After 8 weeks, all mice were overnight-fasted and blood was harvested and centrifuged to obtain serum. Samples of tissue and organ were collected after the mice were euthanized. All animal procedures were performed in accordance with the Guidelines for Care and Use of Laboratory Animals of Anhui University of Chinese Medicine and approved by the Animal Ethics Committee of Anhui University of Chinese Medicine.

4.14 Sample collection

Following a period of eight weeks (56 days) during which the mice were administered the drug, the mice were fasted for a period of 12 h. The body weight, abdominal circumference (the thickest part of the body), and body length (from nose to anus) of the mice in each group were measured, and Lee's index was calculated. The mice were anaesthetised and the eyeballs were removed to obtain blood. The heart, liver, spleen, lung and kidney tissues, thymus tissues, epididymis, perirenal and mesenteric fats were taken from the executed mice and photographed. The liver, thymus, epididymal fat,

perirenal fat, and mesenteric fat were weighed, and the organs were immediately washed with pre-cooled saline. Some of the liver and adipose tissue samples were frozen, while the remainder were fixed and preserved.

4.15 Biochemical and histological analysis

The blood lipid profiles of triglyceride (TG), total cholesterol (TC), low-density lipoprotein (LDL-C) and high-density lipoprotein (HDL-C) were detected using a biochemical analyzer (XR200PLUS, Xinrui Medical Equipment Technology Co., Ltd., China).

The collected organs and tissues were fixed with 10% formalin for oil red O staining and H&E staining. The slices were viewed and imaged under the optical microscope (LEICA DM2000 LED, Germany).

4.16 Statistical analysis

Data were presented as mean \pm standard deviation. All values were analyzed using a one-way ANOVA or *t*-test by Graph-Pad Prism 9.5.0 software. *P* values < 0.05 were regarded as statistically significant.

Data availability

The data supporting this article have been included as part of the ESI†

Conflicts of interest

There are no conflicts to declare.

Acknowledgements

This work was supported by the National Natural Science Foundation of China (82304324), the Open Fund of High-level Key Discipline of Chemistry of Chinese Medicine of the State Administration of Traditional Chinese Medicine, Anhui University of Chinese Medicine (HKDCCM2024003), the University Collaborative Innovation Project in Anhui Province (GXXT-2022-066), Anhui University of Chinese Medicine Scientific Research Fund Project (2021efy1c01), and the High-level Talents Support Project of Anhui University of Chinese Medicine (2022rczd011).

References

- M. Blüher, Obesity: global epidemiology and pathogenesis, *Nat. Rev. Endocrinol.*, 2019, **15**, 288–298.
- M. I. Goran, G. D. C. Ball and M. L. Cruz, Obesity and risk of type 2 diabetes and cardiovascular disease in children and adolescents, *J. Clin. Endocrinol. Metab.*, 2003, **88**, 1417–1427.
- A. Worthmann, J. Ridder, S. Y. L. Piel, I. Evangelakos, M. Musfeldt and H. Voß, *et al.*, Fatty acid synthesis suppresses dietary polyunsaturated fatty acid use, *Nat. Commun.*, 2024, **15**, 45.
- C. Postic and J. Girard, Contribution of de novo fatty acid synthesis to hepatic steatosis and insulin resistance: lessons from genetically engineered mice, *J. Clin. Invest.*, 2008, **118**, 829–838.
- M. López, S. Tovar, M. J. Vázquez, R. Nogueiras, R. Señaris and C. Diéguez, *et al.*, Sensing the fat: fatty acid metabolism in the hypothalamus and the melanocortin system, *Peptides*, 2005, **26**, 1753–1758.
- D. Lee and J. Y. Imm, Antiobesity Effect of Tricin, a Methylated Cereal Flavone, in High-Fat-Diet-Induced Obese Mice, *J. Agric. Food Chem.*, 2018, **66**, 9989–9994.
- Q. Sun, X. Xing, H. Wang, K. Wan, R. Fan and C. Liu, *et al.*, SCD1 is the critical signaling hub to mediate metabolic diseases: Mechanism and the development of its inhibitors, *Biomed. Pharmacother.*, 2024, **170**, 115586.
- X. Palomer, J. Pizarro-Delgado and E. Barroso, *et al.*, Palmitic and oleic acid: the yin and yang of fatty acids in type 2 diabetes mellitus, *Trends Endocrinol. Metab.*, 2018, **29**, 178–190.
- Y. Akazawa, S. Cazanave, J. L. Mott, N. Elmi, S. F. Bronk and S. Kohno, *et al.*, Palmitoleate attenuates palmitate-induced Bim and PUMA up-regulation and hepatocyte lipoapoptosis, *J. Hepatol.*, 2010, **52**, 586–593.
- V. Shettar, S. Patel and S. Kidambi, Epidemiology of Obesity and Pharmacologic Treatment Options, *Nutr. Clin. Pract.*, 2017, **32**, 441–462.
- Jyotshna, P. Khare and K. Shanker, Mangiferin: A review of sources and interventions for biological activities, *BioFactors*, 2016, **42**, 504–514.
- G. Xiang, S. Guo, N. Xing, Q. Du, J. Qin and H. Gao, *et al.*, Mangiferin, a Potential Supplement to Improve Metabolic Syndrome: Current Status and Future Opportunities, *Am. J. Chin. Med.*, 2024, **52**, 355–386.
- J. Li, M. Liu, H. Yu, W. Wang, L. Han and Q. Chen, *et al.*, Mangiferin Improves Hepatic Lipid Metabolism Mainly Through Its Metabolite-Norathyriol by Modulating SIRT-1/AMPK/SREBP-1c Signaling, *Front. Pharmacol.*, 2018, **9**, 201.
- S. Mei, M. Perumal, M. Battino, D. D. Kitts, J. Xiao and H. Ma, *et al.*, Mangiferin: a review of dietary sources, absorption, metabolism, bioavailability, and safety, *Crit. Rev. Food Sci. Nutr.*, 2023, **63**, 3046–3064.
- J. Zivković, K. A. Kumar, R. Rushendran, K. Ilango, N. M. Fahmy and H. A. S. El-Nashar, *et al.*, Pharmacological properties of mangiferin: bioavailability, mechanisms of action and clinical perspectives, *Naunyn-Schmiedeberg's Arch. Pharmacol.*, 2024, **397**, 763–781.
- G. L. Amidon, H. Lennernäs, V. P. Shah and J. R. Crison, A theoretical basis for a biopharmaceutic drug classification: the correlation of in vitro drug product dissolution and in vivo bioavailability, *Pharm. Res.*, 1995, **12**, 413–420.
- M. Liu, Y. Liu, Y. Ge, Z. Zhong, Z. Wang and T. Wu, *et al.*, Solubility, Antioxidation, and Oral Bioavailability Improvement of Mangiferin Microparticles Prepared Using the Supercritical Antisolvent Method, *Pharmaceutics*, 2020, **12**, 90.
- P. Thiengkaew, S. Thanitwatthanarak, S. Srisala, B. Jittorntrum, R. Chunhabundit and P. Chitprasert, Response

- surface optimization of microfluidic formulations of nanobilosomes for enhancement of aqueous solubility, digestive stability, and cellular antioxidant activity of mangiferin, *Food Chem.*, 2021, **351**, 129315.
- 19 M. A. El Hamd, M. El-Maghrabey, S. Almaghwash, R. El-Shaheny and G. Magdy, Self-ratiometric fluorescence approach based on plant extract-assisted synthesized silver nanoparticles for the determination of vanillin, *Microchim. Acta*, 2023, **191**, 16.
 - 20 H. Li, J. Huang, B. Yang, T. Xiang, X. Yin and W. Peng, *et al.*, Mangiferin exerts antitumor activity in breast cancer cells by regulating matrix metalloproteinases, epithelial to mesenchymal transition, and β -catenin signaling pathway, *Toxicol. Appl. Pharmacol.*, 2013, **272**, 180–190.
 - 21 M. O. Sim, H. J. Lee, D. E. Jeong, J. H. Jang, H. K. Jung and H. W. Cho, 6'-O-acetyl mangiferin from *Iris rossii* Baker inhibits lipid accumulation partly via AMPK activation in adipogenesis, *Chem.-Biol. Interact.*, 2019, **311**, 108755.
 - 22 J. Zheng, H. Xiao, Y. Duan, B. Song, C. Zheng and Q. Guo, *et al.*, Roles of amino acid derivatives in the regulation of obesity, *Food Funct.*, 2021, **12**, 6214–6225.
 - 23 F. Xiao and F. Guo, Impacts of essential amino acids on energy balance, *Mol. Metab.*, 2022, **57**, 101393.
 - 24 C. P. Landowski, X. Song, P. L. Lorenzi, J. M. Hilfinger and G. L. Amidon, Floxuridine amino acid ester prodrugs: enhancing Caco-2 permeability and resistance to glycosidic bond metabolism, *Pharm. Res.*, 2005, **22**, 1510–1518.
 - 25 M. Curran and S. Noble, Valganciclovir, *Drugs*, 2001, **61**, 1145–1150.
 - 26 W. B. Guo, H. Zhang, W. Q. Yan, Y. M. Liu, F. Zhou and D. S. Cai, *et al.*, Design, synthesis, and biological evaluation of ligustrazine - betulin amino-acid/dipeptide derivatives as anti-tumor agents, *Eur. J. Med. Chem.*, 2020, **185**, 111839.
 - 27 E. Cai, X. Song, M. Han, L. Yang, Y. Zhao and W. Li, *et al.*, Experimental study of the anti-tumour activity and pharmacokinetics of arctigenin and its valine ester derivative, *Sci. Rep.*, 2018, **8**, 3307.
 - 28 G. R. Wu, B. Xu, Y. Q. Yang, X. Y. Zhang, K. Fang and T. Ma, *et al.*, Synthesis and biological evaluation of podophyllotoxin derivatives as selective antitumor agents, *Eur. J. Med. Chem.*, 2018, **155**, 183–196.
 - 29 Y. Hou, S. Fan, H. Zhang, Y. Gu, X. Yu and B. Li, Pharmacokinetic study of mangiferin in rat plasma and retina using high-performance liquid chromatography, *Mol. Vision*, 2010, **16**, 1659–1668.
 - 30 J. Han, J. Yi, F. Liang, B. Jiang, Y. Xiao and S. Gao, *et al.*, X-3, a mangiferin derivative, stimulates AMP-activated protein kinase and reduces hyperglycemia and obesity in db/db mice, *Mol. Cell. Endocrinol.*, 2015, **405**, 63–73.
 - 31 Y. Hosny, N. S. Abutaleb, M. Omara, M. Alhashimi, M. M. Elsebaei and H. S. Elzahabi, *et al.*, Modifying the lipophilic part of phenylthiazole antibiotics to control their drug-likeness, *Eur. J. Med. Chem.*, 2020, **185**, 111830.
 - 32 E. Z. Mohammed, N. M. El-Dydamony, E. A. Taha, M. N. Taha, A. B. M. Mehany and H. A. Abdel Aziz, *et al.*, Design, synthesis, and molecular dynamic simulations of some novel benzo[d]thiazoles with anti-virulence activity against *Pseudomonas aeruginosa*, *Eur. J. Med. Chem.*, 2024, **279**, 116880.
 - 33 X. Wang, X. Shao, M. Wang, Y. Li, T. Geng and Y. Wang, *et al.*, Design, synthesis, anticancer activity evaluation and molecular dynamics study of pyrazine N-oxide-based SHP2 allosteric inhibitors, *Eur. J. Med. Chem.*, 2025, **293**, 117687.
 - 34 W. S. Liu, J. F. Zhao, X. J. Guo, S. Z. Lu, W. Li and W. Z. Li, Design, synthesis, activity and molecular dynamics studies of 1,3,4-thiadiazole derivatives as selective allosteric inhibitors of SHP2 for the treatment of cancer, *Eur. J. Med. Chem.*, 2023, **258**, 115585.
 - 35 S. Li, J. h. Pan, X. Hu, Y. Zhang, D. M. Gong and G. W. Zhang, Kaempferol inhibits the activity of pancreatic lipase and its synergistic effect with orlistat, *J. Funct. Foods*, 2020, **72**, 104041.
 - 36 S. Bhagat, M. Arfeen, L. Adane, S. Singh, P. P. Singh, A. K. Chakraborti and P. V. Bharatam, Guanlythiourea derivatives as potential antimalarial agents: Synthesis, in vivo and molecular modelling studies, *Eur. J. Med. Chem.*, 2017, **135**, 339–348.
 - 37 F. J. Cimas, M. Á. De la Cruz-Morcillo, C. Cifuentes, N. Moratalla-López, G. L. Alonso and E. Nava, *et al.*, Effect of Crocetin on Basal Lipolysis in 3T3-L1 Adipocytes, *Antioxidants*, 2023, **12**, 1254.
 - 38 Y. Jiang, S. J. Ding, F. Li, C. Zhang, D. X. Sun-Waterhouse and Y. L. Chen, *et al.*, Effects of (+)-catechin on the differentiation and lipid metabolism of 3T3-L1 adipocytes, *J. Funct. Foods*, 2019, **62**, 103558.
 - 39 M. Kudo, M. Gao, M. Hayashi, Y. Kobayashi, J. Yang and T. Liu, *Ilex paraguariensis* A.St.-Hil. improves lipid metabolism in high-fat diet-fed obese rats and suppresses intracellular lipid accumulation in 3T3-L1 adipocytes via the AMPK-dependent and insulin signaling pathways, *Food Nutr. Res.*, 2024, **62**, 103558.
 - 40 D. Zahn, B. Schilling and S. M. Kast, Enhancement of the Wolf Damped Coulomb Potential: Static, Dynamic, and Dielectric Properties of Liquid Water from Molecular Simulation, *J. Phys. Chem. B*, 2002, **106**, 10725–10732.
 - 41 O. Trott and A. J. Olson, AutoDock Vina: Improving the speed and accuracy of docking with a new scoring function, efficient optimization, and multithreading [J], *J. Comput. Chem.*, 2010, **31**, 455–461.
 - 42 M. S. Valdés-Tresanco, M. E. Valdés-Tresanco, P. A. Valiente and E. Moreno, gmx_MMPBSA: A New Tool to Perform End-State Free Energy Calculations with GROMACS, *J. Chem. Theory Comput.*, 2021, **17**, 6281–6291.
 - 43 J. Li, X. Wang, X. Meng, X. Zhou, H. Huang and Y. Feng, *et al.*, Geraniin targeting CaMKK2 inhibits lipid accumulation in 3T3-L1 adipocytes by suppressing lipogenesis, *Chem.-Biol. Interact.*, 2023, **372**, 110364.
 - 44 A. B. Petersen, G. Konotop, N. H. M. Hanafiah, P. Hammershøj, M. S. Raab and A. Krämer, *et al.*, Strategies for improving the solubility and metabolic stability of griseofulvin analogues, *Eur. J. Med. Chem.*, 2016, **116**, 210–215.